A Dissertation Submitted to the
University of Surrey Physics Department
in partial fulfilment of the degree of
Master of Physics

An Upgrade of the TITAN-EBIT High Voltage Operation for Investigations into Decay Rate Modifications by Highly Charged Ions

Matthew Foster

Department of Physics
Faculty of Engineering and Physical Sciences
University of Surrey
Guildford, Surrey, GU2 7XH

TRIUMF
4004 Wesbrook Mall
Vancouver, BC V6T 2A3, Canada

January 9, 2017

Abstract

The TITAN-EBIT was primarily integrated into the TITAN experimental setup to overcome mass measurement precision limitations, but its ability to create highly-charged ions at rest in a laboratory environment also introduced new research opportunities. By changing electronic configurations to modify decay rates, previously unmeasured decay modes can be observed via in-trap spectroscopy. Decay-rate modifications due to high charge states are particularly interesting for the nucleosynthesis of isotopes in stars and stellar explosions as they affect reaction mechanics and influence the pathways of stellar evolution.

In order to obtain higher charge states necessary for investigations into decay-rate modifications, an upgrade of the TITAN-EBIT high voltage operation from 7 kV to 62 kV was performed. The new potentially available higher charge states required adaption of the TITAN switchyard electrode potential configurations for EBIT extraction, and the new values were obtained from SIMION simulations. This dissertation details the upgrade process and its accompanying work which enables the extension of the TITAN experimental program towards the in-trap spectroscopy of decay modifications for nuclei up to bare terbium (Z=65).

Acknowledgements

I would like to express my appreciation and thanks to Dr Iris Dillmann, who's continual patience and support, and engaging teaching has guided me through my research project and the writing of this dissertation. I would also like to express my gratitude to Dr Carla Babcock and Renee Klawitter, for providing their valued expertise, suggestions and encouragement. I extend my thanks to Mel Good for providing invaluable technical support and to the whole TITAN collaboration for their support of my work.

Contents

List of Tables

List of Figures

Chapter 1

Introduction and Background

1.1 The TRIUMF Facility

TRIUMF is Canada's National Laboratory for Nuclear and Particle Physics and Accelerator-based Science. Located on the south campus of the University of British Columbia on the west coast of Vancouver, the 12.6 acre site accommodates facilities committed to research in nuclear and particle physics, nuclear medicine, materials science, and accelerator and detector physics [1].

TRIUMF operates the world's largest cyclotron which can accelerate hydrogen ions up to energies of 500 MeV. The cyclotron comprises two semi-circular metal electrodes normal to a magnetic field to which an alternating current is applied. Negatively charged hydrogen ions from an ion source delivered off-centre into the cyclotron undergo circular motion due the uniform magnetic field and are accelerated by the potential difference between electrodes. Spiral shaped electromagnets ensure that higher energy ions remain in the magnetic field for longer due to their increased radial distance from the centre of the cyclotron, a feature required for the ions to continue on the intended trajectory. 11 μm thick graphite foils, inserted at radii corresponding to desired energies, strip the accelerated H^- ions of their electrons. With their charge polarity switched, the H^+ ions change direction and are guided out of the cyclotron, producing a high-intensity (up to 100 μA)

proton beam. Whilst proton acceleration typically achieves an extraction efficiency of approximately 80-90%, TRIUMF's method of accelerating H^- ions but extracting H^+ ions attains an efficiency of 99.999% [1, 2].

1.2 The ISAC-TITAN Facility

TRIUMF's cyclotron is capable of sending four proton beams of varying energies to different facilities across the site. The primary beam line is connected to the "Isotope Separator and Accelerator" (ISAC) facility, an isotope separation on-line (ISOL) facility that provides radioactive isotopes for nuclear astrophysics, nuclear structure, material science, and fundamental symmetries experiments. Radioactive isotopes are produced at one of two target stations by spallation and fragmentation reactions induced by impinging 475-500 MeV protons on a solid target material, such as uranium carbide (UC_x) [2]. The targets are coupled with either a surface ionisation, resonance ionisation laser or plasma ion source resulting in a radioactive ion beam (RIB) that is extracted and separated by a high resolution magnetic mass-separator with a resolving power of $\frac{m}{\Delta m} \approx 2500$ [3, 4]. The extracted beam (E$\leq$60keV) [5] is then transported in the low-energy beam transport (LEBT) beamline to the ISAC-I experimental hall (Figure 1.1). The extraction yield from the target is dependent on the target chemistry, and not all elements can be extracted in high enough quantities for measurements (Figure 1.2). If an isotope can be chemically and thermally extracted into the ion source before it decays, elements with lower ionisation energies like alkali and earth alkali metals have higher extraction efficiencies.

A facility of particular interest for this dissertation is "TRIUMF's Ion Traps for Atomic and Nuclear science" (TITAN), an experimental setup for studies of short-lived isotopes by use of ion traps (Figure 1.3). Capable of precisely measuring the mass of short-lived (ms) unstable isotopes to an accuracy of $\frac{\delta m}{m} \leq 10^{-8}$, TITAN broadens and aids our knowledge and understanding of nuclear structure and nucleosynthesis. TITAN

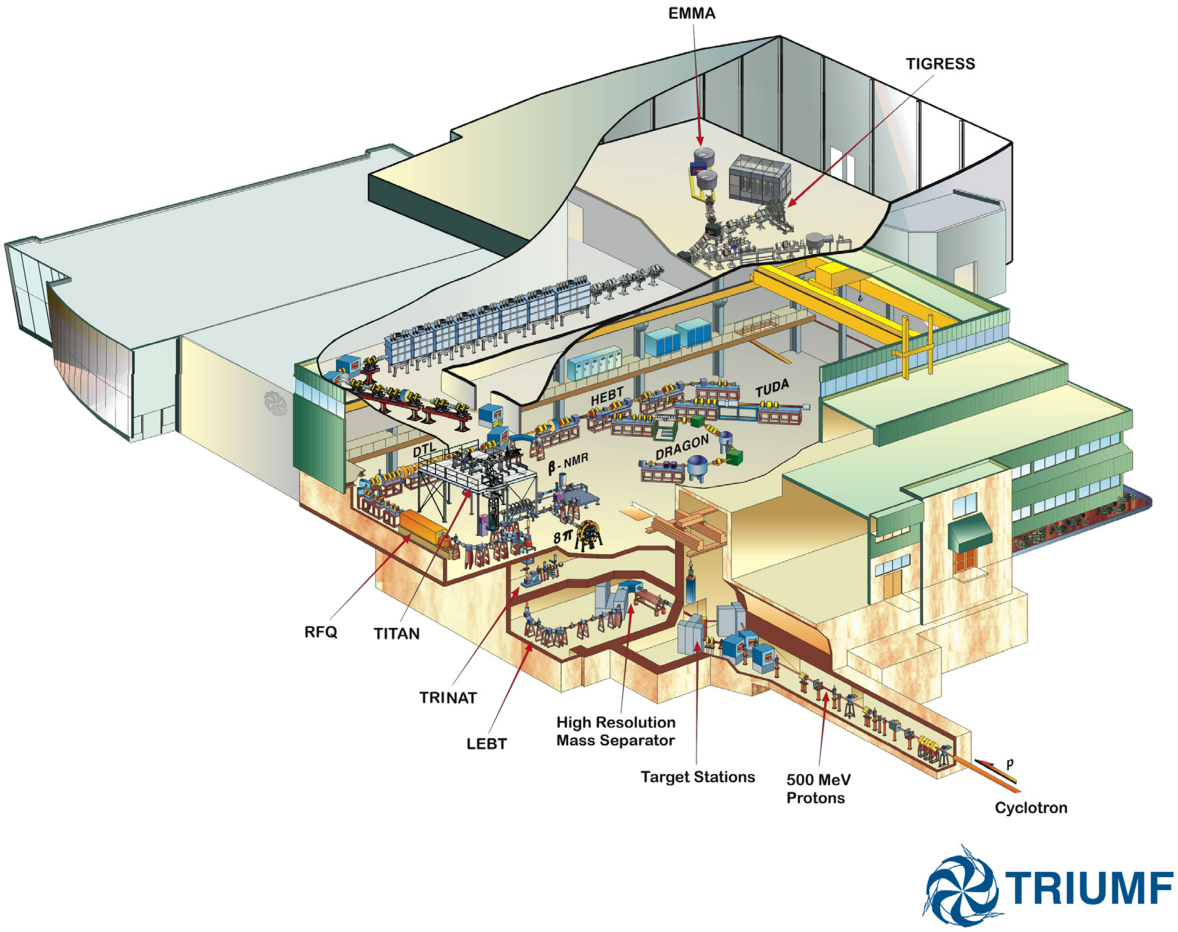

Figure 1.1: The TRIUMF-ISAC facility. Figure from Ref. [6].

currently comprises three on-line traps (RFQ, MPET, EBIT) whilst a fourth (CPET) is being commissioned off-line.

1.2.1 RFQ (Radio Frequency Quadrupole Cooler and Buncher Trap)

TITAN receives the ISAC beam of singly-charged ions (SCI) at the RFQ cooler and buncher trap. Any beam incident on a buffer gas loses energy via collisions, cooling in three dimensions until it reaches equilibrium. Dispersion eventually results in a loss of beam requiring that a DC electric field gradient be applied along the principal axis to accelerate the cooled and slowed ions, however additional fields are required to limit dis-

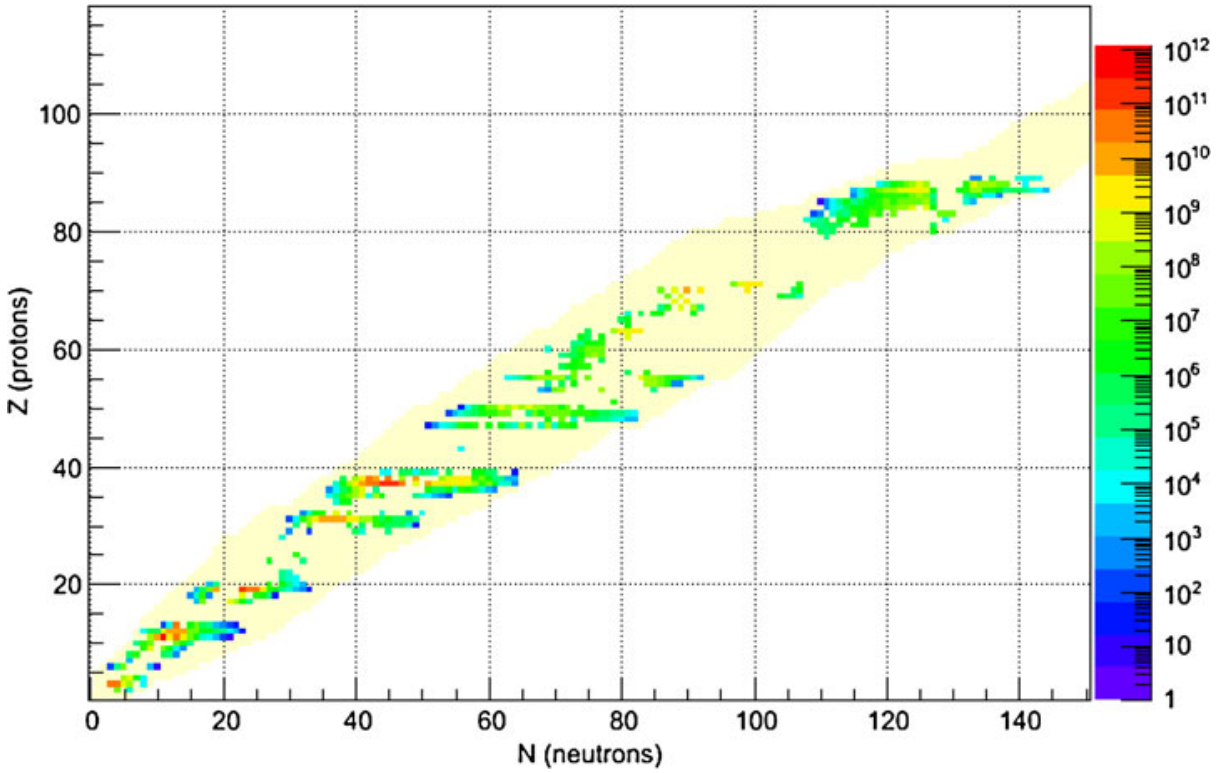

Figure 1.2: ISAC maximum radioactive ion beam yields. The yellow background indicates all known isotopes. Figure from Ref. [7].

persion in the transverse axes. An RFQ radially traps ions in a time-dependent electric field consisting of alternating polarities applied to longitudinal electrodes in a quadrupole arrangement. TITAN cools and bunches the ions for only tens of ms, filling the RFQ with an inert gas and using segmented electrodes to capture ions in a potential well before ejecting them towards an electrostatic beam switchyard [5, 9, 10]. The RFQ has a space-charge limit of $\sim 10^6\, e$ [11].

1.2.2 MPET (Measurement Penning Trap)

TITAN's precision mass measurements are performed in the MPET using the Time-of-Flight Ion-Cyclotron-Resonance (ToF-ICR) technique [8]. A 3.7 T homogenous magnetic field along the longitudinal direction of the trap confines ions radially and results in a radial magnetron motion [4]. Penning traps comprise three hyperboloid electrodes: surfaces of revolution forming a ring and two endcaps (Figure 1.4), which confine ions axially and

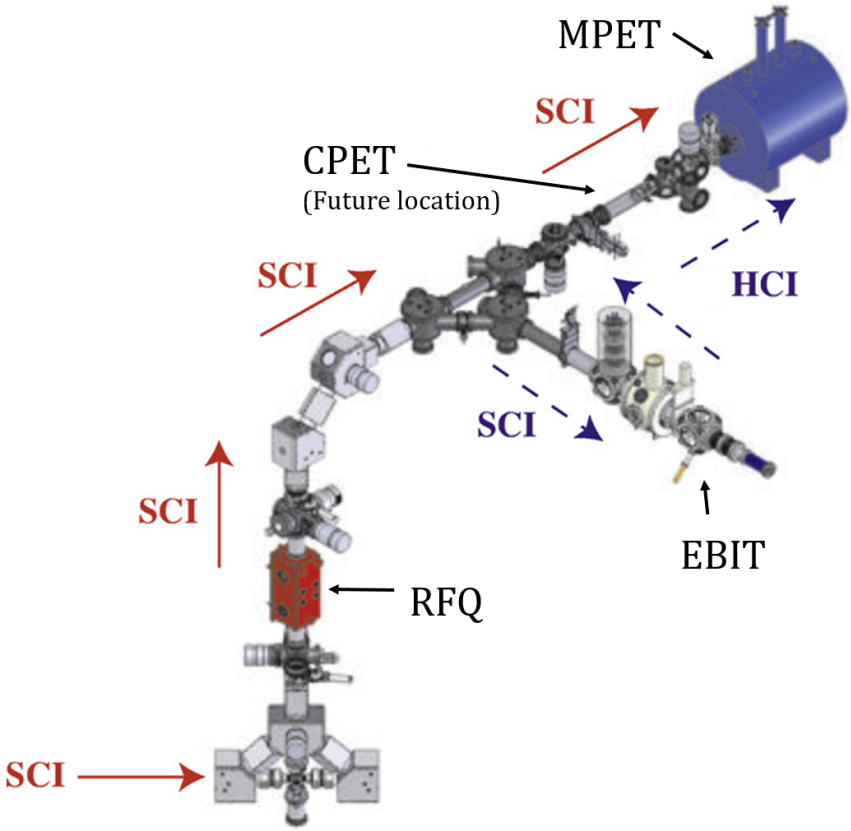

Figure 1.3: The TITAN experimental setup. MPET measures either singly-charged ions (SCI) received directly from ISAC or highly-charged ions (HCI) charge bred at the EBIT. Figure adapted from Ref. [8].

induce simple harmonic motion along the endcap axis when an electrostatic quadrupole field is applied. In combination with the magnetic field, the electric field induces a second radial reduced cyclotron motion [8, 9, 12] (Figure 1.5). A second applied oscillating quadrupole field excites the ions and couples the reduced cyclotron and magnetron frequencies. Conversion between the reduced cyclotron and magnetron motions occurs when the frequency of the applied field is resonant with the cyclotron frequency. For an ideal trap the cyclotron frequency (ν_c) is equal to the sum of the reduced cyclotron (ν_+) and magnetron (ν_-) eigenfrequencies, and is inversely proportional to the mass of the ion m [8, 12]:

$$\nu_c = \nu_+ + \nu_- = \frac{q\ e\ B}{m}, \tag{1.1}$$

where q is the ion's charge state, e the charge of an electron, and B the magnetic field strength. An increase in kinetic energy at resonance minimises an ion's time-of-flight (ToF) once released from the trap. Ions are then detected at a micro-channel plate (MCP) detector comprising a dense array of small, parallel capillaries (≈10 μm diameter) in which electron cascades that amplify the signal are induced by impinging ions. Obtained from a ToF vs quadrupole field frequency plot, the resonant frequency is equal to the cyclotron frequency and used in Eq. 1.1 to precisely calculate the mass of the ion [9, 10, 12].

TITAN can perform mass measurements on SCI with the RFQ and MPET alone, but can increase its sensitivity by charge-breeding to higher charge states via an "Electron Beam Ion Trap" (EBIT).

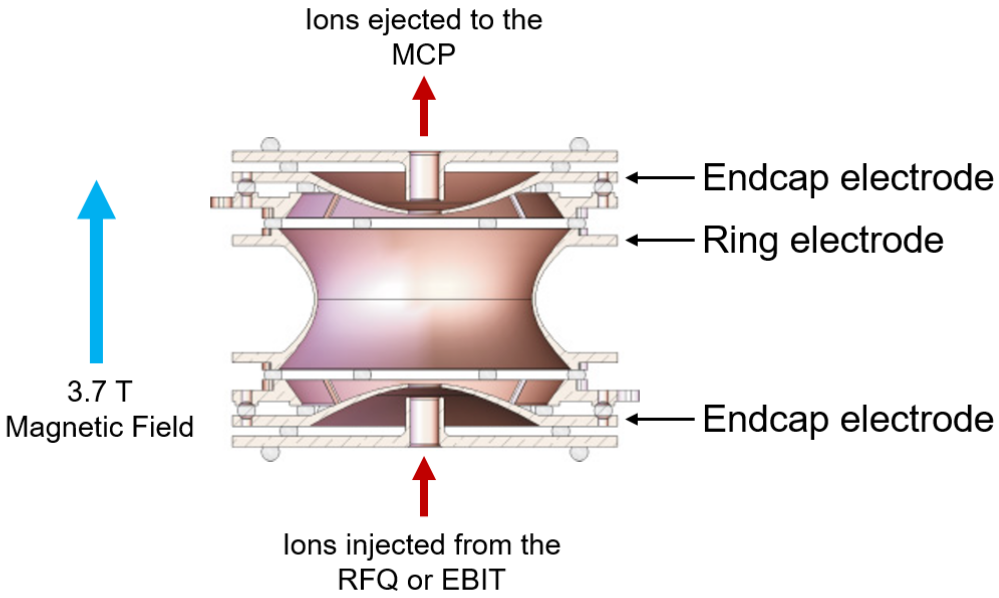

Figure 1.4: The Penning trap design of the TITAN-MPET. Figure adapted from Ref. [12].

1.2.3 EBIT (Electron Beam Ion Trap)

An Electron Beam Ion Trap (EBIT) was fully integrated into the TITAN facility in 2008 [14] to overcome MPET mass measurement precision limitations. The statistical

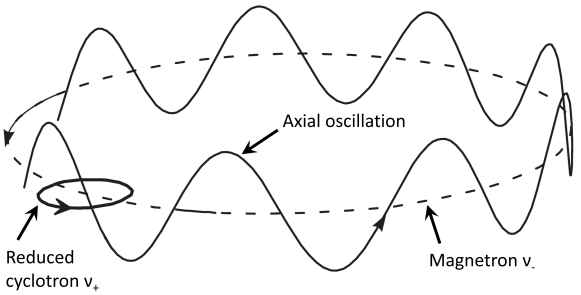

Figure 1.5: Penning trap ion eigenmotions. Figure adapted from Ref. [13].

uncertainty of Penning trap mass measurements [14],

$$\frac{\delta m}{m} \propto \frac{m}{qB} \frac{1}{T_{RF}} \frac{1}{\sqrt{N}}, \tag{1.2}$$

is dependent on the magnetic field strength in the trap B, the excitation time T_{RF}, the number of ions N and the charge state q. The excitation time of unstable short-lived isotopes is limited by their half-lives, and neither the magnetic field strength nor the number of ions can be readily increased. Thus the most efficient reduction of uncertainty is achieved by increasing the charge state q. Ions undergo charge breeding in the EBIT where electrons are removed by electron impact ionisation. Further detail on EBITs is provided in Chapter 3.

1.2.4 CPET (Cooler Penning Trap)

Despite the reduction in statistical uncertainty by charge breeding, the resulting increased energy spread of the charge-bred beam to 10−100 eV/q decreases the injection efficiency into the MPET and broadens the ToF resonance. A standard process of cooling is the use of a buffer gas [4, 15], however this results in charge-exchange reactions when charge states are greater than 1^+ or 2^+. TITAN's Cooler Penning Trap (CPET), an ion trap presently being commissioned off-line, therefore cools ions by electron cooling. In a strong magnetic field electrons self-cool by emitting synchrotron radiation. CPET utilises this property by confining HCI in a trap filled with electrons in nested potentials, cooling

them via Coulomb interactions. Cooled ions are extracted to the MPET before electron-ion recombination becomes dominant [16].

Chapter 2

Nuclear Theory

2.1 Radioactive Decay

A radioactive decay is a nuclear transformation resulting in a nucleus losing energy via emission of radiation [17]. All decay modes can be classified as either nucleon conversion, a transition of states via photon emission, or nucleon emission based on the processes involved in the decay.

2.1.1 Nucleon Conversion

Decay modes involving the conversion of protons and neutrons whilst the total number of nucleons A remains the same are called "β decays". β-decay modes occur via the weak interaction and utilise one of three primary decay processes:

$$n \rightarrow p + e^- + \bar{\nu_e} \qquad \beta^- \text{ decay} \tag{2.1}$$

$$p \rightarrow n + e^+ + \nu_e \qquad \beta^+ \text{ decay} \tag{2.2}$$

$$p + e^- \rightarrow n + \nu_e \qquad \text{(Orbital) Electron Capture} \tag{2.3}$$

The continuous energy distribution of β particles (electrons or positrons, Figure 2.1) shows that the decay is a three-body process. The additional decay particle (neutrino)

is electrically neutral to conserve electric charge and has spin $\frac{1}{2}$ to conserve angular momentum. The sum of the linear momenta of the β particle and the nucleus shows that the third particle carries energy but has near-zero mass, it thus travels at almost the speed of light with its total energy equal to its kinetic energy. All β decay particles are created out of the decay energy and do not already exist in the atom [18], in contrast to α decay.

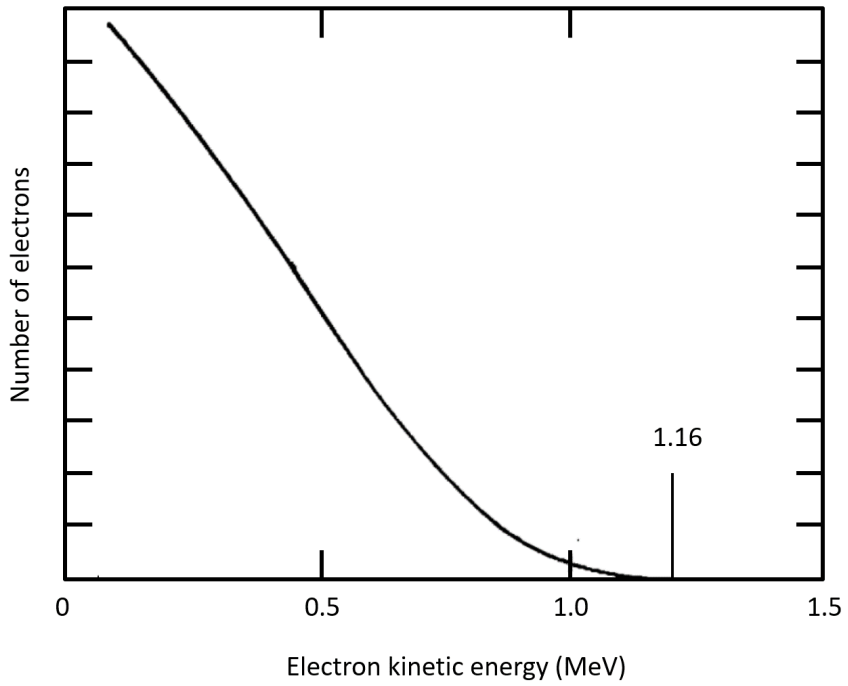

Figure 2.1: Continuous β^- energy distribution of ^{210}Bi β-decay. Figure from Ref. [18].

Of particular interest for this dissertation is "Orbital Electron Capture" (EC) (Figure 2.2) whereby a parent nucleus typically captures an electron from the K shell, resulting in the conversion of a proton to a neutron and the emission of a neutrino,

$$ {}^{A}_{Z}X_N + e^- \rightarrow {}^{A}_{Z-1}X'_{N+1} + \nu_e. \tag{2.4} $$

Orbital EC is a two-body decay, and the spectrum of the emitted neutrino is thus monoenergetic. The vacancy left in the K shell is filled by an electron that transitions down from a higher atomic level thereby emitting a characteristic X ray. Compared to the

spherical K shell, the dumbbell shape of the L shell results in less overlap of the nucleus and L electron wavefunctions, making their capture less likely.

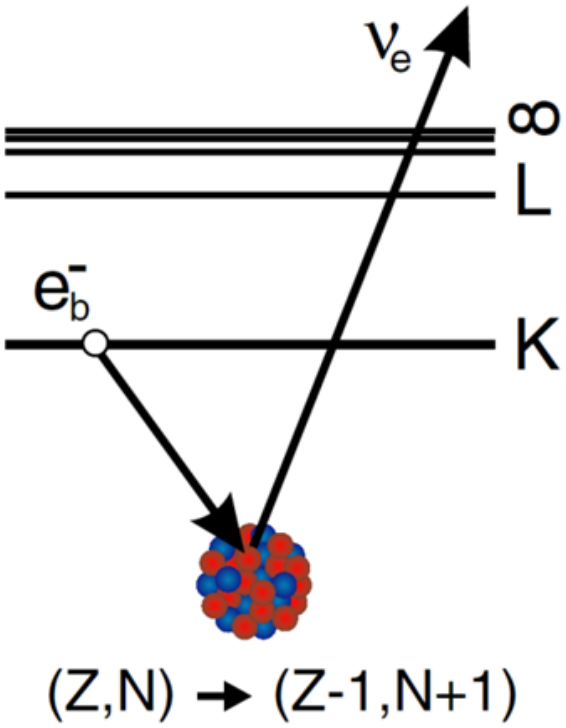

Figure 2.2: Orbital electron capture. Figure from Ref. [19].

Fermi theory of β-decay

The strength of the coupling between a transition's initial and final states, and therefore the transition probability, is determined by Fermi's Golden Rule [20]:

$$W = \frac{2\pi}{\hbar} \left|\langle f|\hat{O}|i\rangle\right|^2 \rho_f, \tag{2.5}$$

where ρ_f is the number of neutrino final states per unit energy and $\hat{O}$ the weak interaction operator. The allowed approximation assumes that each decay particle carries away zero orbital angular momentum ($l = 0$), so the change in total nuclear spin $\Delta I = I_f - I_i$ is equal to the coupled spins of the decay particles in order to conserve angular momentum. Both the neutrino and β particle have spin $\frac{1}{2}$. Parallel spins ($S = 1$) result in so-called

"Gamow-Teller" decays where initial and final states are coupled by one unit of angular momentum, $I_i = I_f + 1$ [21]. "Fermi decays" are due to anti-parallel spins ($S = 0$) and there is no change in angular momentum $\Delta I = |I_i - I_f| = 0$. The $l = 0$ approximation forbids parity changes since the parity π is $(-1)^{-l}$. The selection rules for allowed β-decays are therefore,

$$\Delta I = 0, 1 \quad \Delta\pi = 0.$$

"Superallowed" $0^+ \rightarrow 0^+$ transitions are purely Fermi decays. The small affect on the nucleus' wavefunction by the transition means the decays are a useful tool for testing our understanding of electroweak interactions [22]. Although the selection rules imply that all other transitions are entirely forbidden, they only indicate relative decay rates. For example the first-forbidden decay ($l = 1$) could have a change in total angular momentum of ΔI = 0, 1 or 2 but parity violation makes the transition less likely and results in longer half-lives [18].

Decay	**ΔI**	**Δπ**
Superallowed	$0^+ \rightarrow 0^+$	no
Allowed	0, 1	no
First Forbidden	0, 1, 2	yes
Second Forbidden	1, 2, 3	no
Third Forbidden	2, 3, 4	yes
Fourth Forbidden	3, 4, 5	no

Table 2.1: Angular momentum and parity selection rules.

2.1.2 Nucleon Emission

Some decay modes result in the emission of nucleons. Many heavy nuclei (A > 210) decay via α-decay,

$$^{A}_{Z}X_N \rightarrow ^{A-4}_{Z-2}X'_{N-2} + \alpha. \tag{2.6}$$

In 1909 Rutherford demonstrated that the emitted α particle is a Helium nucleus (He^{2+}). Due to its comparatively small mass, the total kinetic energy released by the

decay, Q_α, is large. Figure 2.3 displays the simplified potential energy of an α particle (assumed already pre-formed in the nucleus) and daughter nucleus system. A potential well of depth $-V_0$ exists inside the nucleus and a Coulomb potential with a maximum value at the surface of the nucleus prevents the α particle from escaping. Classically, an α particle cannot escape the nucleus with an energy less than the Coulomb barrier, however the particle's wavefunction results in a small chance of it tunnelling through the barrier. The small probability of tunnelling accounts for why α particles are still emitted but not all emitted immediately [18].

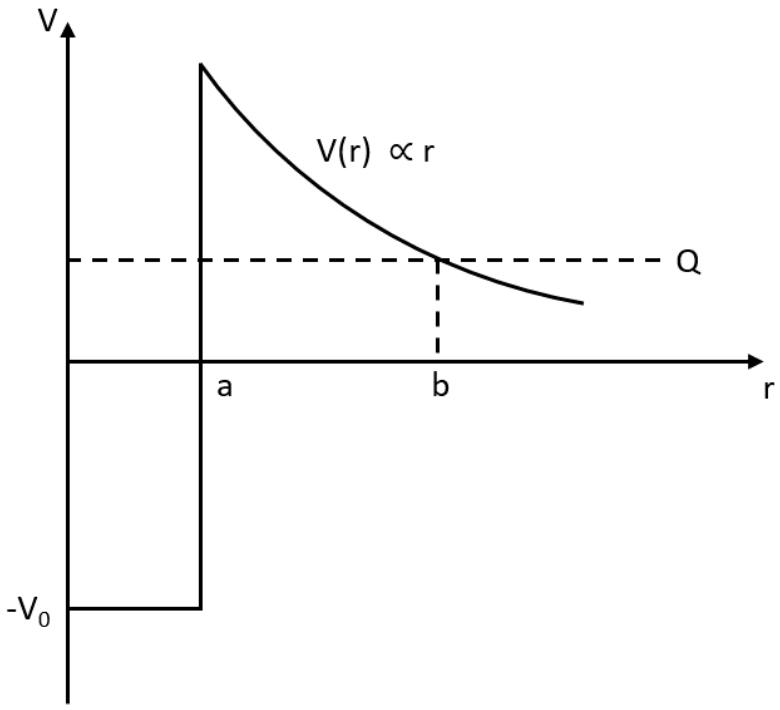

Figure 2.3: α-particle potential energy as a function of separation distance. A potential well of depth $-V_0$ exists inside the nucleus ($r < a$) and the Coulomb potential decreases exponentially beyond the surface. The potential at b is equal to the decay Q-value. Figure from Ref. [18].

2.1.3 Transition of States

Most nuclear reactions leave the daughter nucleus in an excited state that proceeds to decay to its ground state. The decay releases an energy equal to the difference in energy of the states, typically in the range 0.1–10 MeV [18]. The decay energy is distributed between the kinetic energy of the recoiling daughter nucleus and an emitted γ ray, though the energy of the recoil is so small that the decay energy may be considered as solely that of the γ ray.

Another decay mode involving a transition of states is "Internal Conversion" and occurs when the wavefunctions of an excited nucleus and an orbital electron overlap,

$$ {}^{A}_{Z}X^{*}_{N} \rightarrow {}^{A}_{Z}X^{+}_{N} + e^{-} \rightarrow {}^{A}_{Z}X_{N}. \tag{2.7} $$

The excitation energy is transferred radiationless to the electron which proceeds to escape the atom, leaving a vacancy in the previously occupied shell. These monoenergetic electrons are called "conversion electrons". The subsequent de-excitation of higher lying electrons to fill the vacancy emits an X ray. In contrast to β decay, the emitted electron was not created from the decay energy, but rather already existed in the atomic shell and is emitted with a discrete energy corresponding to the ionisation energy of the respective shell.

2.2 Nucleosynthesis

Other than the lightest elements (H, He, Li), which were formed moments after the Big Bang, all matter in the universe is created in stars and during stellar explosions. Due to their respective reaction Q values, atoms lighter than the iron group nuclei are created by fusion but heavier atoms must proceed via alternate processes, as displayed by Figure 2.4. Iron group nuclei are the fusion limit because of their average 8.8 MeV/nucleon binding

energy. If the total mass of the fusion reactant nuclei is greater than the product nucleus the reaction will yield energy, but the smaller binding energies of nuclei with Z > 26 make their fusion reactions to heavier nuclei energetically unfavourable.

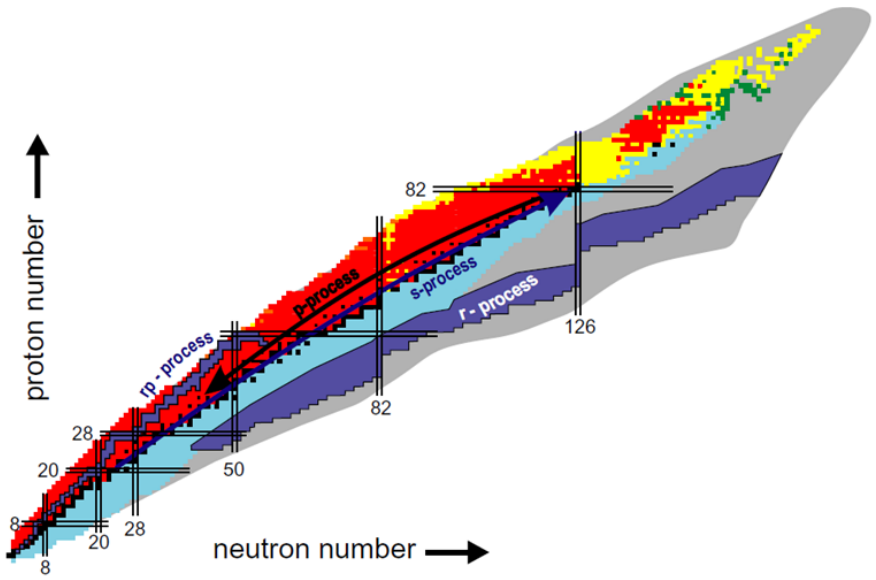

Figure 2.4: The chart of nuclides and astrophysical nucleosynthesis processes. Yellow, red, blue and green nuclei predominantly decay by α-, β^+-, β^--decays and fission, respectively. Grey nuclides are predicted to exist but have not yet been observed in the laboratory. Figure from Ref. [19].

Stars are formed by the gravitational collapse of regions of interstellar dust. The denser regions increase in mass by accreting gas from the surrounding cloud and the continual addition of mass and proceeding collapse results in an increase in temperature. If the mass of a protostar is great enough the core will become sufficiently hot ($\sim 10^6$ K) to initiate hydrogen fusion to ^{4}He which will establish a stable, long-lasting hydrostatic equilibrium when the outward force of the radiation pressure equals the inward force of gravity. As hydrogen is burned and its supply becomes more limited the reduced radiation pressure causes the core to compress under its own gravity, and the resulting increase in temperature ignites the helium and establishes a new hydrostatic equilibrium. The process continues by burning heavier elements in phases until the elements are too heavy to burn at the given core temperature. The mass of the star dictates the heaviest elements it can burn and how long it remains in each burning phase: lower-mass stars (mass $< 8M_\odot$) burn

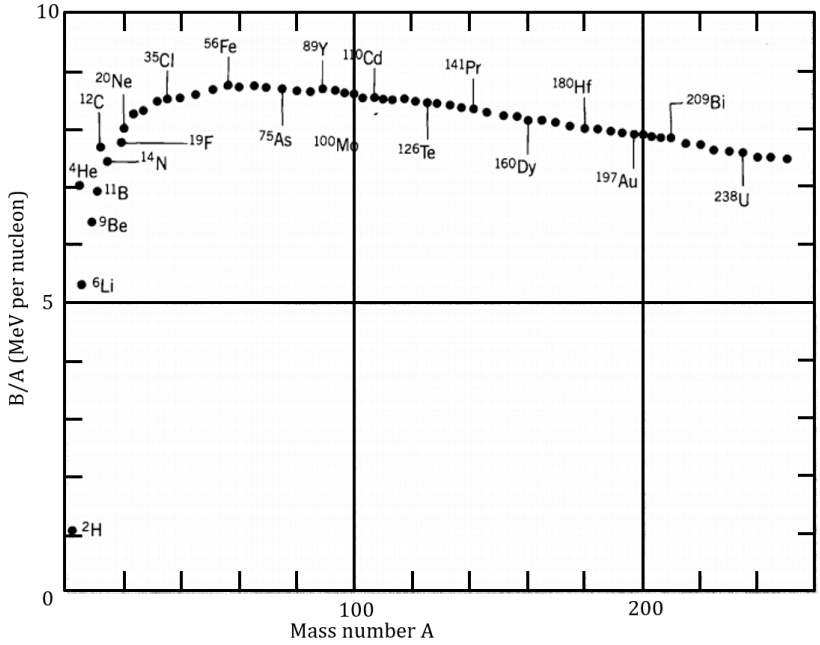

Figure 2.5: Binding energy per nucleon. Figure from Ref. [18].

H and He but the slower fusion rates due to the colder core temperatures result in longer phase lifetimes, however the higher core temperatures of massive stars (mass $> 8M_{\odot}$) result in a fast fusion rate leading to a shorter time in each phase. At several billion Kelvin the core temperature of massive stars is sufficient to ignite the advanced burning phases (C, Ne, O and Si) which produce isotopes up to the iron-group elements with ^{56}Ni in the core that decays to ^{56}Fe. Since fusion cannot occur beyond A = 56 the outward directed force decreases and finally the gravitational core collapse takes over. During a "core collapse supernova" the temperature increases to 10^{11} K forming neutrons in the core and releasing 10^{46} J of energy via reversed β-decay [23]. Neutron degeneracy in the core rebounds the implosion and the energy expands as a shockwave through the outer layers of the star and ignites "explosive burning phases" for a few seconds. The energy quickly dissipates but facilitates processes that result in isotopes heavier than ^{56}Fe. The high energy shockwave accelerates particles in the outer layers to high velocities resulting in their full ionisation. Although recombination due to the high electron plasma densities occurs after 1000 s, at later times (few hundred years after the explosion), a reverse

shockwave from the collision of the ejected material with the interstellar medium can again propagate towards the core and reheat the supernova ejecta up to $5{\cdot}10^7$ K. This can lead to re-ionisation of the ejected material (e.g. long-lived ^{44}Ti or other iron-nickel isotopes) up to one-electron systems [24].

Elements heavier than iron and nickel are produced mainly via neutron-capture reactions on long and short timescales compared to the beta-decays and can occur in different astrophysical scenarios. The "slow" neutron capture (s) process produces its neutrons via α-induced reactions on light isotopes like ^{13}C and ^{22}Ne, which leads to a reaction path that runs along the valley of stability up to ^{210}Bi (see Figure 2.4). The "rapid" neutron capture (r) process requires explosive, very neutron-rich scenarios such as core collapse supernova explosions or the merging of neutron stars. With these extreme conditions the reaction path runs far off stability (see Figure 2.4) through mainly as yet unexplored isotopes. When the temperature and neutron density decreases, the neutron-rich nuclei decay back to stability and produce about 50% of the abundances of heavy stable isotopes.

2.2.1 Decay Rate Modification

Early attempts to measure radioactive decay rate modifications by altering electron density resulted in no discontinuity within error [25]. Experiments included varying the environment's temperature, pressure and magnetic fields, but studies were on limited species and all decayed via α- or β-particle emission. The observed abundances of short-lived radioisotopes in the universe, however, suggest that in some cases the decay rate may be slower or faster than that observed terrestrially. The combined high temperatures, electron densities and high velocities of stellar conditions are sufficient to influence some decay rates, resulting in new decay modes that are not easily accessible under terrestrial conditions. For example, thermal population of low-lying excited states can be induced by high stellar temperatures, subsequently decreasing the β- or γ-decay lifetimes if so-called "gateway states" are populated from which the nucleus can decay through an isomeric

state. Isotopes that would otherwise be stable under terrestrial conditions can then become radioactive and open new reaction process routes for the nucleosynthesis processes.

Orbital Electron Capture

Galactic cosmic rays (GCRs) are highly ionised nuclei that travel through the galaxy having likely been accelerated and re-accelerated by supernova explosions. Studies of GCR energy spectra provide an insight into nucleosynthesis but since GCRs interact with atmosphere, measurements are made by detectors outside of Earth's atmosphere [26]. Launched in 1997 on board NASA's "Advanced Composition Explorer" (ACE) spacecraft [27], the "Cosmic Ray Isotope Spectrometer" (CRIS) measured galactic matter composition at energies ranging from 50–500 MeV/nucleon for $2 \leq Z \leq 30$ nuclei impinging on the detector [28]. When compared to the solar system composition ACE-CRIS data demonstrated that there were discrepancies between particular isotope abundances. The comparison of GCR and solar system abundances is shown in Figure 2.6. Primary isotopes that are re-accelerated by supernovae show good agreement, but secondary isotopes that are produced in-flight by spallation and fragmentation reactions disagree and have lower solar system abundances.

Examination of isotopic abundances also revealed some unexpected results with the detection of some short-lived species. The Be, Fe and Co abundance examples in Figure 2.7 show the presence of ^{7}Be, ^{55}Fe and ^{57}Co, species that with half-lives of 53.22 d, 2.744 y and 271.74 d [29], respectively, would be expected to have already decayed before reaching the detector. The presence of short-lived nuclei, the disparity between GCR and solar system compositions and the unlikelihood of unnoticed supernovae close to the detector suggest that supernovae environments influence particular radioactive decay rates.

An explanation of the root cause of the disagreement with prediction was provided by the decay modes of ^{7}Be, ^{55}Fe and ^{57}Co since all decay 100% via orbital electron

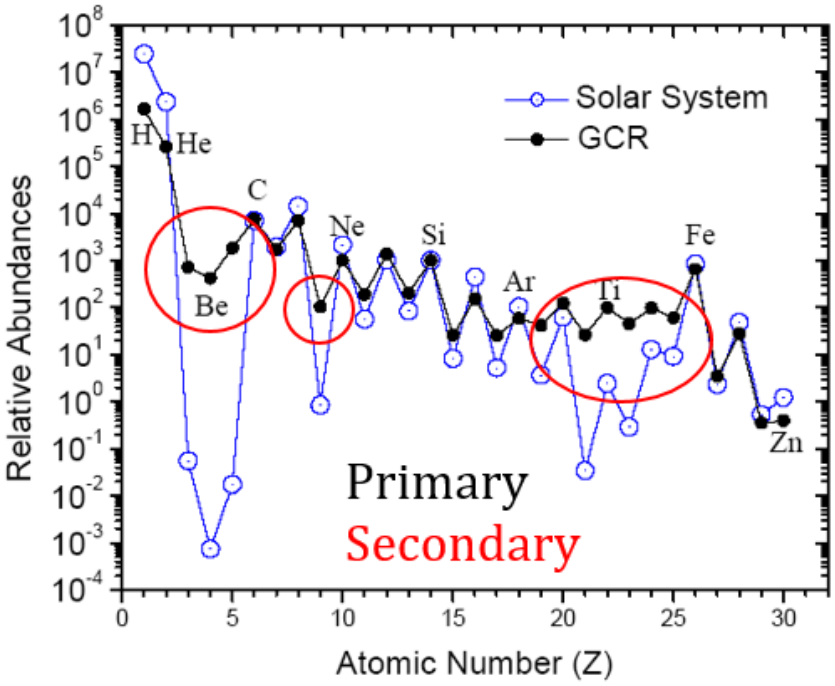

Figure 2.6: Comparison of GCR and solar system abundances. Figure adapted from Ref. [27].

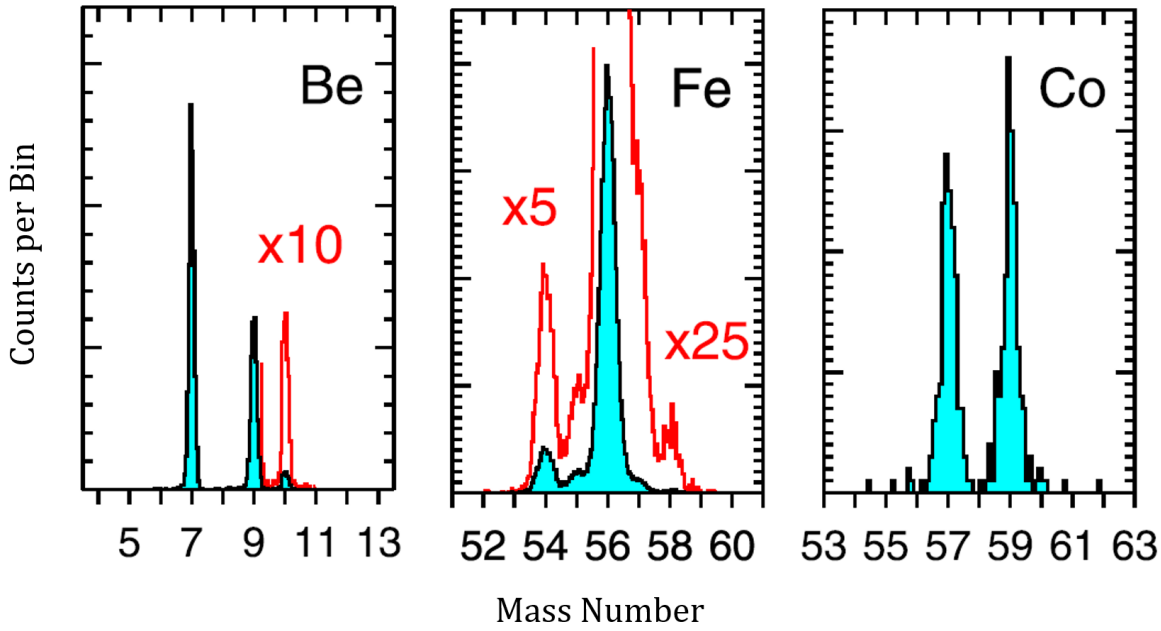

Figure 2.7: GCR isotopic abundances of Be, Fe and Co. Bins with low counts are expanded and shown in red with their multiplication factors displayed. Figure adapted from Ref. [30].

capture and full ionisation thus increases their half-life to infinity. Hot stellar conditions such as supernova explosions and the acceleration of the supernova remnant allow full ionisation of such isotopes, though EC still occurs due to the abundance of free electrons in the continuum that can be captured. A simple interpretation of electronic configurations concludes that an atom that only decays by EC is stable when fully ionised, but a half-filled K shell with one valence electron (H-like state) should have a half-life twice as long as a full shell since the electron density is half. The half-life of the He-like state with two valence electrons should correspond approximately to the terrestrial half-life, with additional consideration for the absence of L shell (n=2) electrons that contribute $\frac{1}{n^3}$. This simple approximation estimates that the half-lives of Helium-like states are $\frac{9}{8}$ of their terrestrial half-lives [11, 31]. An example of the predicted ^{7}Be decay rate modifications is shown in Figure 2.8.

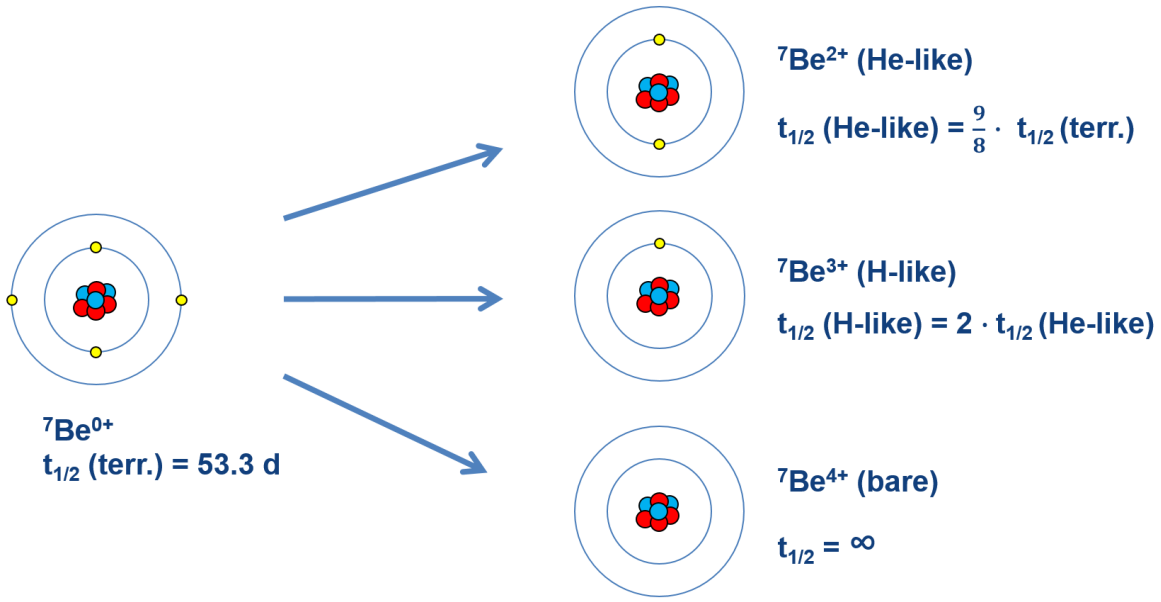

Figure 2.8: ^{7}Be decay rate modification prediction.

EC decay rates have been measured in the Experimental Storage Ring (ESR) at GSI Darmstadt for bare, H- and He-like ^{140}Pr and ^{142}Pm, and bare and H-like ^{122}I [32–34]. Whilst the half-lives for bare and He-like ions agreed with the simple assumption, the

half-lives for H-like ions disagreed and instead had a half-life of $\frac{9}{10}t_{\frac{1}{2}}$(terr.). The solution is that for H-like systems the decay rate depends on the hyperfine structure [21, 33, 35]. For example, the nuclear and electron spins of H-like ^{140}Pr are $I = 1$ for the ground state and $s = \frac{1}{2}$, respectively. They can couple to two hyperfine states $F_i = I \pm s = \frac{3}{2},\ \frac{1}{2}$. Decaying to the ground-state of ^{140}Ce^{58+} via EC the final nuclear spin is reduced to 0 and the emitted neutrino has spin $\frac{1}{2}$ resulting in a $F_f = \frac{1}{2}$ state. Due to the conservation of total angular momentum the $\frac{3}{2}\rightarrow\frac{1}{2}$ transition is twice-forbidden and the main contribution to the decay rate is the allowed $\frac{1}{2}\rightarrow\frac{1}{2}$ transition. The decay rate is dependent on transition probability ratios and initial state statistical weightings.

Using Eq. 2.5 as its foundation, Ref. [35] derives the probability of allowed H-like ion EC decays in terms of He-like EC decay probabilities:

$$I \rightarrow I \pm 1 \qquad W_{He} = \frac{2(I \pm \frac{1}{2}) + 1}{2I + 1}\, W_H, \tag{2.8}$$

$$I \rightarrow I \qquad W_{He} = \frac{2(I\ +\ \frac{1}{2}) + 1}{2I + 1}\, W_H^+ \ +\ \frac{2(I\ -\ \frac{1}{2}) + 1}{2I + 1}\, W_H^-, \tag{2.9}$$

where I is the initial nuclear spin, $\pm$ corresponds to $I\rightarrow I\pm1$ and $W_H^{\pm}$ corresponds to $I\pm\frac{1}{2}\rightarrow I\pm\frac{1}{2}$ transitions. The relative rates predicted by Eqs. 2.8 and 2.9 agree with the empirical values and explain why H-like states with shorter half-lives than He-like states can be observed.

Orbital electron capture hindrance is observed in nature during the hydrogen burning pp-II chain in the core of the Sun. The ^{3}He$(\alpha,\gamma)^7$Be reaction at temperatures of 15.6 million Kelvin in the core of the Sun produces bare ^{7}Be^{4+} which should not decay. The isotope can be observed, however, due to free electron capture which allows the ^{7}Be to decay despite the high core temperature. The isotope is therefore present in the solar neutrino spectrum (Figure 2.9) with two energy peaks that correspond to the ground and excited states of the ^{7}Li daughter nucleus [36–38].

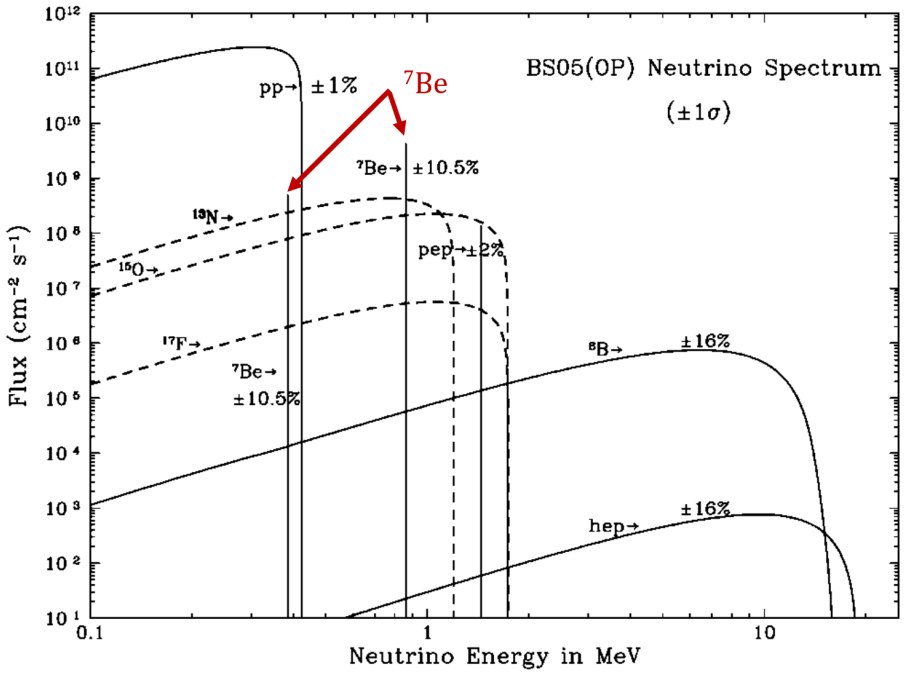

Figure 2.9: Solar neutrino energy spectrum from the BS05 solar model. The two ^{7}Be energy peaks correspond to the ground and excited states of the ^{7}Li daughter nucleus. Figure from Ref. [39].

Bound-state β^- decay

Bound-state β^- decay (β_b) is a weak interaction transition where rather than being emitted into the continuum, a β^- particle is instead emitted into a bound-state of the daughter atom [40]. In neutral atoms, weakly bound states are available but their low-density near the nucleus reduces the statistical weighting of the decay branch. In highly-ionised ions however, transitions into bound states are possible and have higher probabilities. β_b decay was first observed in 1992 in ^{163}Dy^{66+} which in a neutral state is a stable isotope, but has a half-life of 47 days as a bare ion [41]. This behaviour leads to a branching in the reaction path of the slow neutron capure process under stellar conditions. Even more significant is ^{187}Re β_b decay which was first highlighted by Takahashi et al. [42,43]. Although stable whilst neutral, Takahashi noted the full ionisation of ^{187}Re achieved in stellar conditions would permit β_b decay that would influence the total decay rate. Fig-

ure 2.10 displays the ^{187}Re decay scheme. Neutral $^{187}Re^{0+}$ has only one energetically favourable decay mode, but being first-forbidden ($\frac{5}{2}^+ \rightarrow \frac{1}{2}^-$) and having a small Q-value ($Q_\beta = 2.66$ keV) its half-life is 44 Gyr with β_b only contributing 1% to the decay [44,45]. For bare $^{187}Re^{75+}$ ions, emission of a β^- particle into the continuum is forbidden, but with a Q-value of +72.97 keV [44] β_b decay into the K shell is possible with the dominant decay being to the 9.75 keV first excited state. An increase in the number of energetically favourable decay modes and their respective Q-values mean stellar conditions reduce the half-life of ^{187}Re by nine orders of magnitude [44,46]. A ^{187}Re decay rate modification has significant astrophysical implications since the ^{187}Re – ^{187}Os decay was used as a cosmochronometer for dating the age of the Universe.

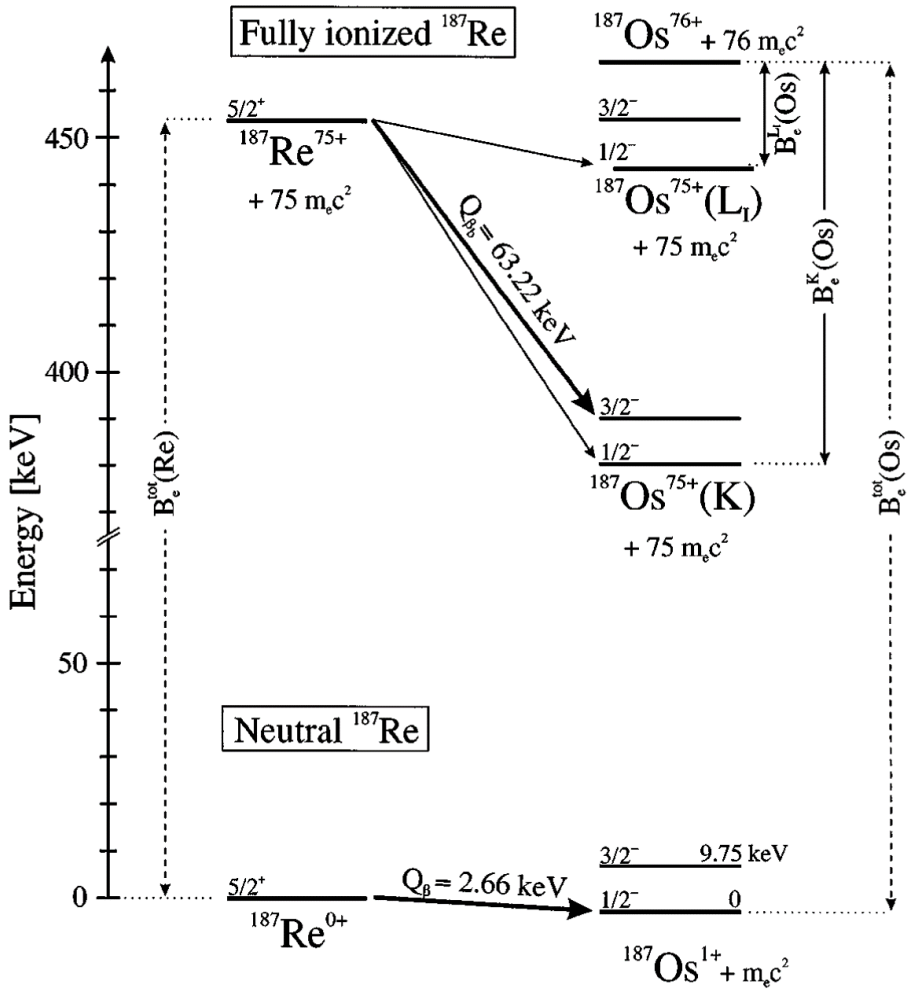

Figure 2.10: ^{187}Re decay scheme. For explanations, see text. Figure from Ref. [44].

Internal Conversion

Internal conversion (IC) occurs when the wavefunctions of an excited nucleus and an orbital electron overlap. This decay mode competes with the de-excitation via a γ ray. Instead of the emission of a γ ray, the energy is transferred "radiationless" to one of the orbital electrons. The electron escapes the atom and a higher lying electron de-excites to fill the vacancy. Full ionisation would thus render atoms stable against internal conversion since there would be no orbital electrons for an excited nucleus to overlap with [47]. Measured cases have so far only involved states that can still de-excite via γ-decay but measurements of bare $^{52m}\mathrm{Mn}^{25+}$, $^{149m}\mathrm{Dy}^{66+}$, $^{151m}\mathrm{Er}^{68+}$ and H-like $^{192m}\mathrm{Os}^{75+}$ at GSI-ESR [47–49] have confirmed the hindrance of IC decay by electronic configuration modifications of up to a factor of 33. Measurements of ^{125}Te [50] have also demonstrated that the lifetime of the $\frac{3}{2}^+$ state increases from 1.48 ns to up to 11 ns when the charge state reaches $q = 45^+$ and above (the effects are measurable in systems with 7 electrons or less) [50].

The hindrance of IC becomes especially interesting in cases where the competing emission of a γ ray is forbidden, as is the case for $0^+ \rightarrow 0^+$ (E0) transitions in nuclei. An upcoming experiment at TITAN intends to probe 2-photon decays by performing in-trap spectroscopy on bare $^{98}\mathrm{Zr}^{40+}$ and $^{98}\mathrm{Mo}^{42+}$ in 0^+ excited states, where the highly competing IC branch has been eliminated by full ionisation [51]. This would mean that in the bare state the nuclei will be "stuck" in a quasi-stable isomeric state that does not exist in the neutral case. However, the nucleus can still decay via the (highly suppressed) two-photon emission. The use of the charge-breeding with the TITAN-EBIT and following spectroscopy offers a much cleaner environment for this rare decay mode compared to regular γ spectroscopy.

Alpha Decay

Electron screening around a nucleus raises the Coulomb barrier and reduces the tunnelling probability, ionisation should therefore result in a higher decay probability. The effects of electron screening are predicted to affect the α-decay half-life of bare ions compared to neutral atoms in the sub-% range, however, any attempts to measure any modifications by electron screening have so far observed no changes due to large statistical errors [52]. In addition the half-lives of many alpha-decaying isotopes are not known to the sub-% level, so any measurement needs also to remeasure the neutral half-lives to a high enough precision before any effect of the reduced electron screening can be observed.

Chapter 3

Electron Beam Ion Trap

High charge states are an important area of astrophysics research due to the effect of lower electron densities on astrophysical decay rates. Although it is difficult to exactly reproduce stellar conditions, recent advancements of electron beam ion traps have made it possible to create HCI at rest in a laboratory environment. Astrophysical environments can have temperatures of tens of million Kelvin up to billions of Kelvin, and ultra-high vacuum conditions but high electron plasma densities in excess of 10^{25} cm^{-2}, whilst the environment inside an EBIT typically corresponds to temperatures of only $\sim$4 K, electron densities which are 10–15 orders of magnitudes lower and ultra-high vacuum (UHV) pressures of 10^{-10} Torr. EBITs produce few-electron, high charge state ions by directing an electron beam at an ion cloud where the impinging electrons sequentially remove electrons from the ions by "electron impact ionisation" (EII) [53, 54].

3.1 The TITAN-EBIT

The TITAN-EBIT (Figure 3.1) was integrated into the TITAN experimental setup in November 2008 to overcome MPET mass measurement precision limitations and comprises three parts: an electron gun, a trap and a collector. Ions are trapped axially by an electrostatic trapping potential created by electrodes in a drift-tube assembly. A magnetic field generated by Helmholtz coils surrounding the drift-tube assembly is centred

on the EBIT's cylindrical line of symmetry and compresses the electron beam, increasing its current density. The resulting electron-beam space-charge potential traps the ions radially [14].

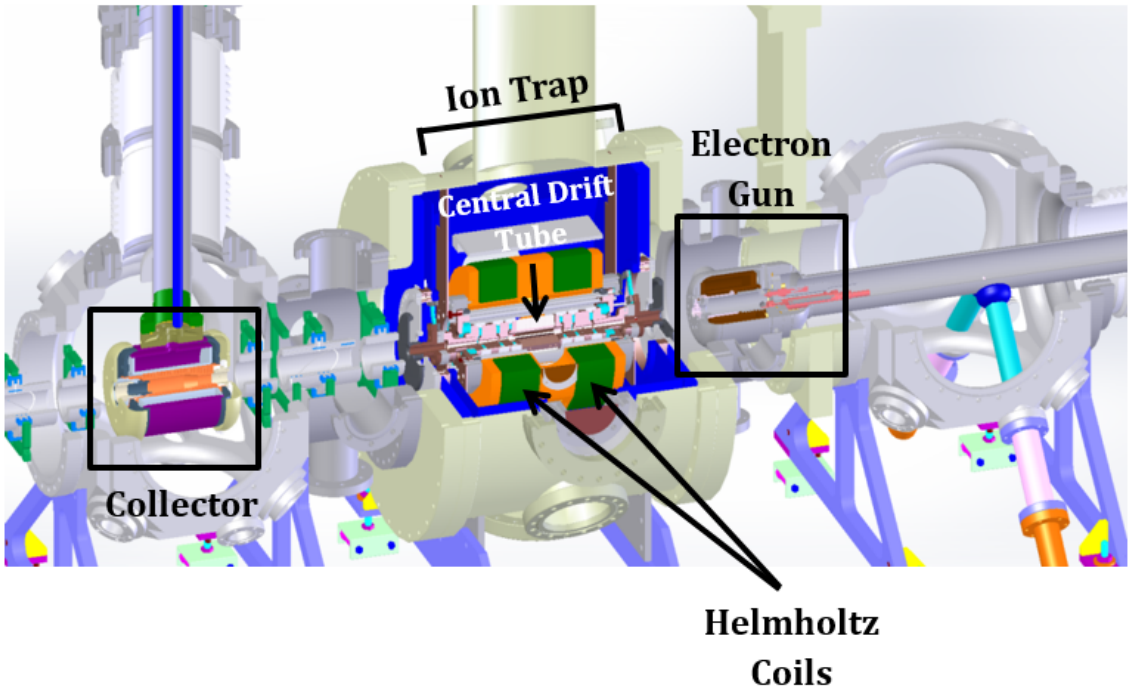

Figure 3.1: The TITAN-EBIT. Figure adapted from Ref. [55].

3.1.1 Electron Beam Production

The EBIT electron gun uses a barium oxide dispenser cathode capable of producing a beam current of 500 mA. In addition to the cathode, the gun assembly also contains a trim coil, soft iron yoke and a bucking coil to reduce the magnetic field strength at the cathode and increase the maximum beam compression by the Helmholtz coils when in the trap [14].

The radius (in μm) of a compressed beam produced by a cathode in a zero-magnetic

field environment, and neglecting thermal effects, is equal to the Brillion radius [56]:

$$r_b = \frac{150}{B}\sqrt{\frac{I_e}{E_e}}, \tag{3.1}$$

where B is the compression magnetic field strength (in T) at the trap, I_e the electron beam current (in A) and E_e the electron beam energy (in keV). However, the cathode dispenses electrons by thermionic emission in an environment not entirely absent of magnetic fields, thus the compressed radius is larger than the Brillion radius.

An alternate radius approximation is the Herrmann radius [56]:

$$r_h = r_b \sqrt{\frac{1}{2} + \frac{1}{2}\sqrt{1 + 4(\frac{8kT_c\ {r_c}^2\ m_e}{e^2\ {r_b}^4\ B^2} + \frac{{B_c}^2\ {r_c}^4}{B^2\ {r_b}^4})}}, \tag{3.2}$$

where kT_c is the electron beam energy at the cathode, r_c the cathode radius, m_e the electron mass, e the charge of an electron and B_c the magnetic field strength at the cathode. The Herrmann radius calculates the radius in which 80% of the beam is contained and serves as a good approximation to the radial region in which the beam charge is held.

3.1.2 Ion Trap

The space charge potential of an electron beam is [56]:

$$V_e(\rho) = V_0(\frac{\rho}{r_h})^2 \qquad \text{if} \quad \rho < r_h \tag{3.3}$$

$$V_e(\rho) = V_0(2\ ln(\frac{\rho}{r_h}) + 1) \qquad \text{if} \quad \rho > r_h \tag{3.4}$$

where ρ is the radial distance of the point of interest to the centre of the beam and V_0 (in V) is:

$$V_0 = \frac{30I}{\sqrt{1 - (\frac{E_e}{511} + 1)^{-2}}} \tag{3.5}$$

where I (in A) and E_e (in keV) are the electron beam current and energy, respectively. Equations 3.3 and 3.4 demonstrate the dependence of the space-charge potential on the electron beam radius and show that the beam generates a radial potential that will radially trap positive ions.

The electron beam is directed through a drift-tube assembly (Figure 3.2) which comprises a series of nine individually biased drift tubes. The configuration of tube potentials (Figure 3.3), in which the central tube is matched approximately to the beam energy and biased to 2 kV relative to the outer tubes, generates a well-defined trapping potential centred on the central tube [14]. The TITAN-EBIT's standard central drift-tube potential is 1950 V with its two adjacent electrodes raised to 2050 V for trapping, which produces a trap depth of $\sim$100 V. During ion bunch injection and extraction the adjacent drift-tube on the collector-side is lowered to 1900 V. The timing of the switching of potentials corresponds to the RFQ-EBIT ion bunch flight time, with the potential being raised when the ions are at the centre of the trap. The trap depth on the central axis in the central drift tube (DT5) is approximately equal to V_t:

$$V_t \approx V_{app} + (V_e(r_{DT4,6}) - V_e(r_{DT5})), \tag{3.6}$$

where V_{app} is the bias of the tubes on either side of DT5 (DT4 and DT6), $r_{DT4,6}$ the radii of DT4 and DT6 and r_{DT5} the radius of DT5. Axial trapping of positive ions occurs if an ion's energy is sufficiently low to be reflected by the higher potential of DT4 and DT6.

Surrounding the drift-tube assembly is a superconducting magnet comprising a pair of Helmholtz coils cooled to 4.5 K to produce a homogeneous 6 T magnetic field. Such a strong magnetic field compresses the electron beam Herrmann radius to approximately 20 μm, thereby increasing the beam's space charge potential [14]. The resulting combination of radial and axial potentials allows an EBIT to trap positive ions centred on a high energy electron beam.

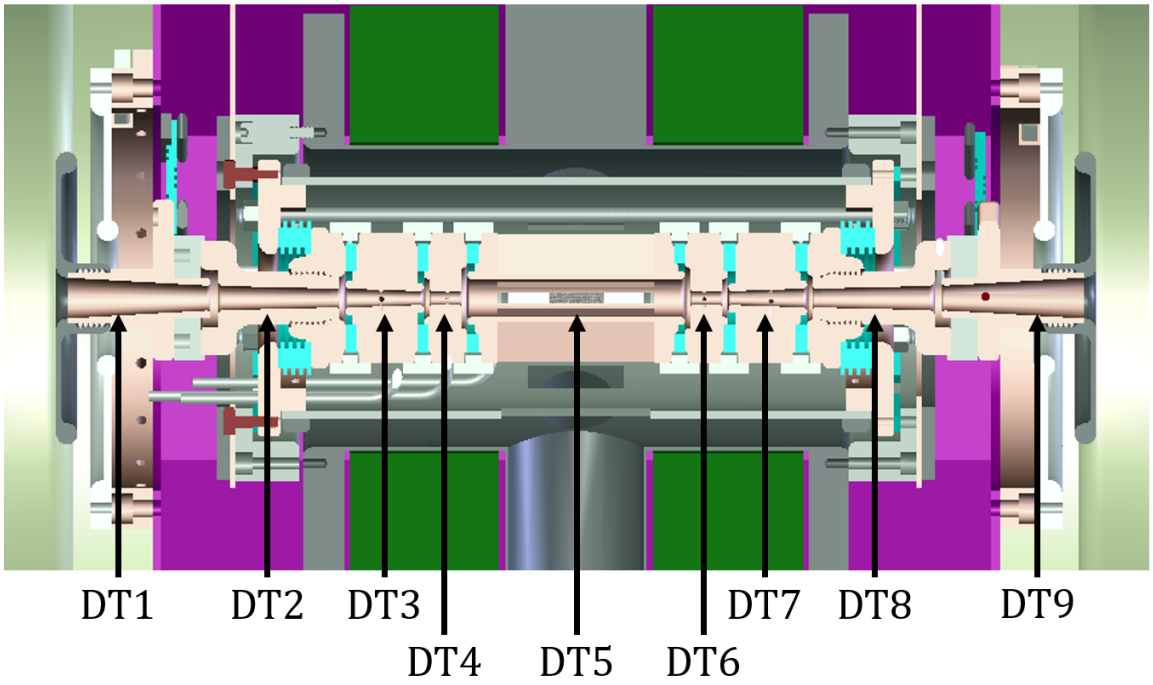

Figure 3.2: Drift-tube assembly. Figure adapted from Ref. [55].

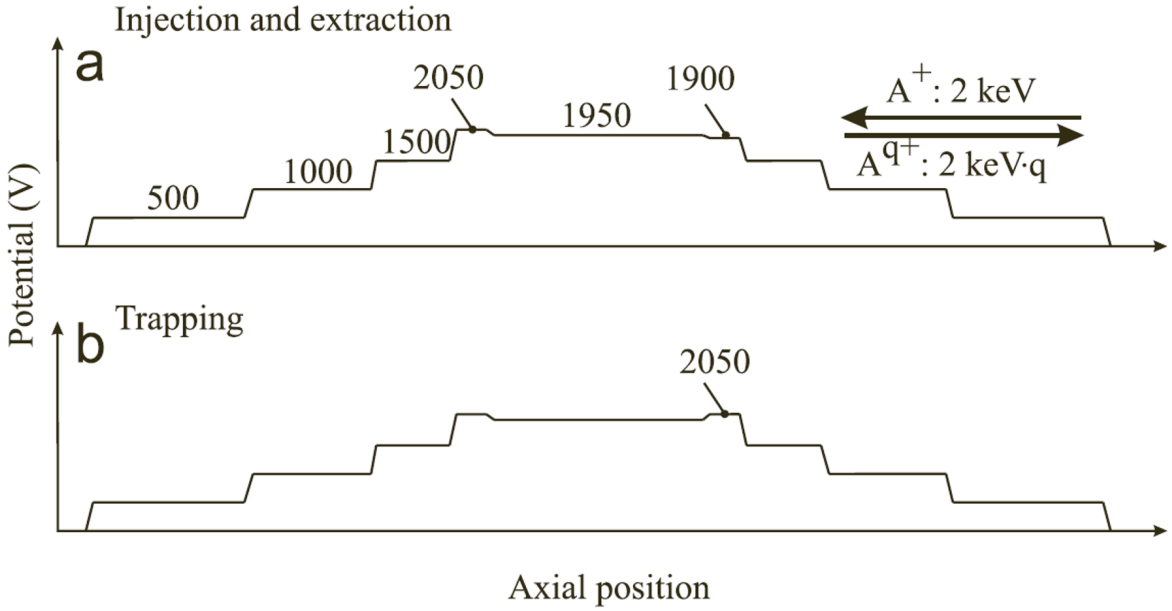

Figure 3.3: Drift-tube potential configurations for (a) injection/extraction and (b) trapping. Figure from Ref. [14].

3.1.3 Collector

A 500 mA electron beam accelerated by a potential of −2 kV requires a collector to dissipate 1 kW of direct current power. The collector is therefore water-cooled and contains various electrodes to defocus the beam. On either side of the collector is an extraction or suppressor electrode, each biased by −400 V relative to the gun. The purpose of the extraction electrode is to defocus the beam onto the collector, and the suppressor electrode prevents electrons from being reflected back into the trap. Since the gun is magnetically shielded to increase compression at the trap, the collector is also shielded to reverse the process. As the magnetic field produced by the trap's Helmholtz coils infringes on the collector assembly a single coil surrounds it to reduce the field strength [14].

3.1.4 Trap Processes

Three main processes that affect the charge-state distribution in the trap region occur in an EBIT (Figure 3.4).

Electron Impact Ionisation (EII)

An EBIT creates HCI by electron impact ionisation whereby the electron beam sequentially knocks off electrons from an atom if the beam energy is greater than the atom's ionisation energy [57]. It has been empirically determined that the energy of impinging electrons is required to be more than twice the ionisation energy to ensure ionisation since the cross section increases with energy.

If the concentration of ions in the trap becomes too high the ion cloud begins to neutralise the electron beam space charge, reducing the radial trapping potential and limiting the obtainable charge states [56]. This effect is called compensation.

Radiative Recombination

In addition to losing electrons, ions can also capture electrons. Radiative recombination occurs when an ion regains an electron and forms an excited ion with a reduced charge state that then de-excites and emits a photon of an energy corresponding to the transition [57]. The recombination cross-section is approximately proportional to the inverse of the interaction energy, thus electrons at higher energies have smaller recombination rates [56].

Charge Exchange

In order for an EBIT to store HCI it is essential that the trap remains in a high vacuum to minimise charge exchange. Charge exchange (Eq. 3.7) is an interaction between positive ions and neutral atoms that results in the exchange of electrons.

$$A^{q+} \; + \; B^{0+} \rightarrow A^{(q-m)+} \; + \; B^{m+} \tag{3.7}$$

Interaction cross-sections are proportional to the charge state so to maintain high charge states the level of residual gases in the trap must be kept at a minimum.

Since EBIT charge breeding produces a charge state distribution (Figure 3.5) and capture of more than one ion species in the MPET adversely affects the precision of mass measurements (Eq. 1.2), the EBIT parameters are set to dominate the desired charge state. For HCI mass measurements at TITAN, a mass to charge ratio of approximately $A/q = 10$ is normally used.

3.1.5 In-Trap Decay Spectroscopy

The TITAN-EBIT was installed to both decrease the relative uncertainty of MPET precision mass measurements and perform in-trap decay spectroscopy. To study HCI at rest the central drift-tube contains seven radial aperture slits that serve as viewports for one

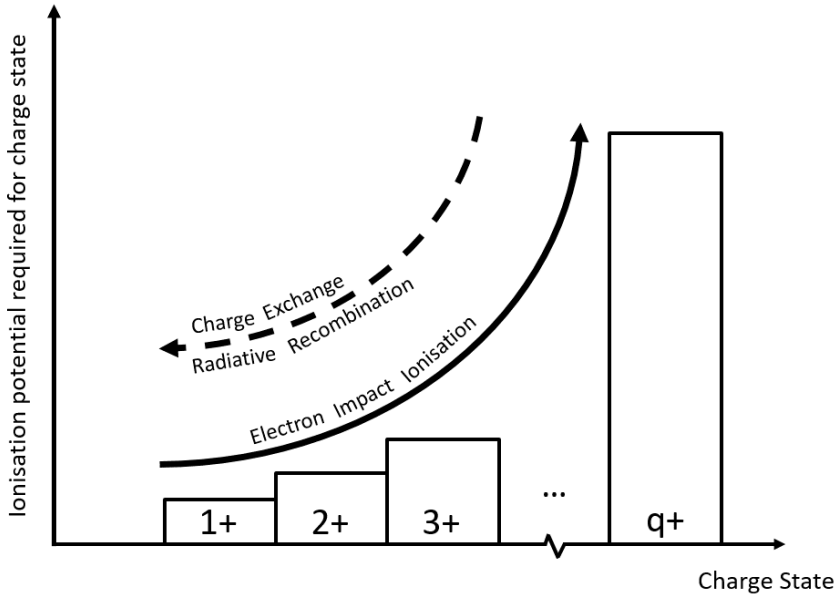

Figure 3.4: In-trap processes.

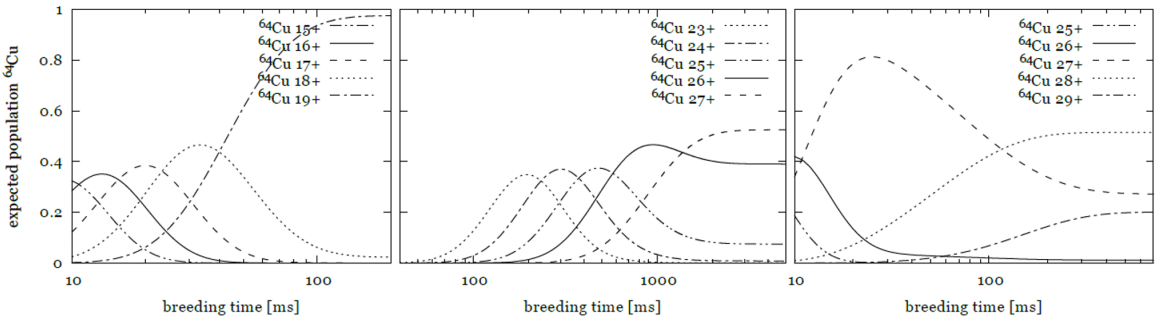

Figure 3.5: Simulated ^{64}Cu Charge Breeding Charge-State Distributions. Figure from Ref. [11].

high-purity Ge (HPGe) and six Si(Li) detectors for spectroscopic measurements (Figure 3.6). Each port has a high-purity Be window to minimise X-ray absorption and when mounted onto the ports the detectors have a solid angle acceptance of ∼2% [58].

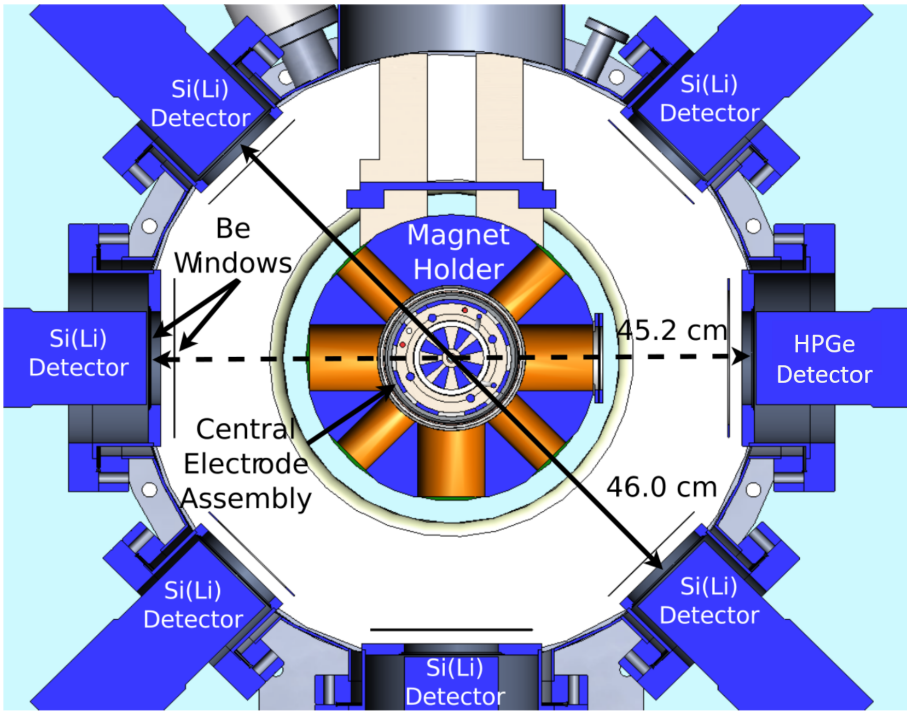

Figure 3.6: Ion trap cross-section. Figure adapted from Ref. [2].

3.1.6 High Voltage Operation

The ionisation potential associated with higher charge states increases exponentially, therefore EBITs must operate at high voltages in order to study very highly charged ions. The design specifications of the TITAN-EBIT support a maximum operating voltage of 62 kV, but safety restrictions have so far limited its maximum high voltage to 7 kV. The highest heavy-ion charge states previously achieved were an average of $q = 26 - 32$ for ^{124}Cs with an electron beam current of 85 mA and electron energy of 2 keV [58]. The upgrade of the EBIT high voltage operation described in this dissertation will allow safe operation at voltages up to 65 kV so as to perform in-trap decay spectroscopy on higher charge states and heavier ions, and to increase the precision of TITAN mass measurements. Operating at 62 kV the TITAN-EBIT will theoretically provide access to bare ions up to Z = 65. The TITAN group already has approval for experiments that explore the change of EC rates of Ne-, He- and H-like charge states of ^{64}Cu, and the 2 photon decays of bare $^{98}Zr^{40+}$ and $^{98}Mo^{42+}$, HCIs that were unobtainable prior to the upgrade.

Chapter 4

Simulations

The low-energy beam received by TITAN at the TITAN-RFQ is cooled to a temperature nearing the thermal energy of the buffer gas, and bunched before being extracted and sent either directly to the MPET for mass measurements, or to the EBIT for charge breeding. Charge bred ions are either extracted to the MPET or observed in the trap. RFQ extraction to the EBIT or MPET, and EBIT extraction to the MPET requires that TITAN have an electrostatic beam switchyard to direct extracted beams to each trap. Bender and steerer electrodes alter the beam trajectory and the beam properties are modified by electrostatic quadrupoles that focus and defocus the beam along its transverse axes. The electrode potential configurations for EBIT injection/extraction are established empirically by adjusting electrode values along the beamline to converge on a maximum transmission. The injection process is reversed for extraction, but the increased charge states after charge breeding modify the electric fields required and the injection electrode values have to be modified to account for this for extraction. Due to a beamline diagnostics deficiency a maximum transmission might only be a local maximum. An understanding of the processes occurring in the switchyard permits better system optimisation, therefore the switchyard is simulated to visualise the beam trajectory and identify issues along the beamline.

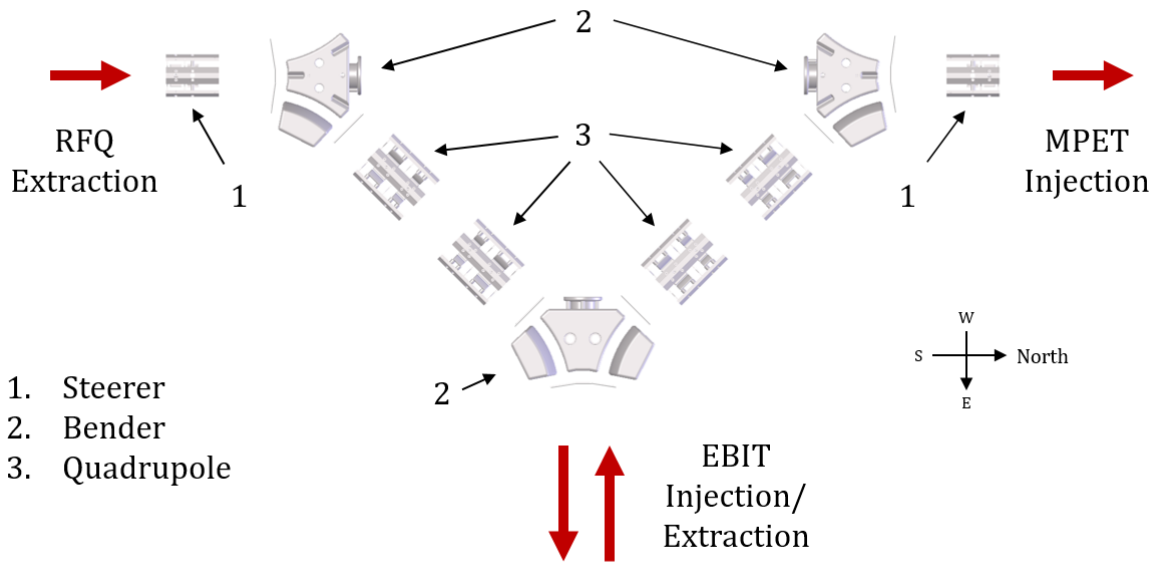

Figure 4.1: TITAN electrostatic beam switchyard CAD model.

4.1 Simulation Method

The electrostatic beam switchyard is simulated in SIMION: an ion optics simulation software package that calculates the trajectories of ions through electric and magnetic fields. SIMION calculates field potentials by assuming zero charge volume density and using the potentials at the electrodes as boundary conditions to solve the Laplace equation via finite difference methods. The Laplace equation defines the potential at a point in terms of the potentials of its surrounding points [59]:

$$\nabla^2 V = \nabla \cdot \nabla V = 0, \tag{4.1}$$

$$E = \nabla V = (\frac{\delta V}{\delta x})i + (\frac{\delta V}{\delta y})j + (\frac{\delta V}{\delta z})k, \tag{4.2}$$

$$\nabla^2 V = \nabla \cdot E = \frac{\delta E_x}{\delta x} + \frac{\delta E_y}{\delta y} + \frac{\delta E_z}{\delta z} = 0. \tag{4.3}$$

SIMION solves (refines) the potentials and creates a potential array of equally spaced points that form either two-dimensional squares or cubic grids. The fields within the array are defined by the gradient of the potentials. The refined potential arrays are inputted into an optics workbench volume as potential array instances. Ions are flown through the workbench volume with their trajectories calculated from the fields they encounter since an electric field (E) is the force (F_E) per charge (q),

$$F_E = qE. \tag{4.4}$$

4.2 Beam Property Measurements

It is beneficial to run simulations with beam properties that replicate measurements because they can demonstrate processes that might realistically occur along the beamline. The beam properties of an extracted EBIT beam were previously measured in 2015 (Figure 4.2) [60]. An Allison detector, positioned along the EBIT longitudinal beam axis to directly measure extracted beams, measured the rms emittance of a beam with an energy of $E_{beam} = 2180$ eV/q as $\varepsilon_{rms} = 8.47\ \pi \cdot \text{mm} \cdot \text{mrad}$.

4.3 Emittance

The trajectory of a single particle can be calculated by solving linear equations of motion, but whilst individual particle trajectories are useful for accelerator design, features of beam dynamics are better explained when the beam is described as a collective motion of particles [61, 62]. Particles are each represented by a single point in six-dimensional phase space ($x,\ p_x,\ y,\ p_y,\ z,\ p_z$), the region in phase space occupied by a beam is the "emittance". Neglecting coupling between axes, the emittance (ε) in each dimension is defined as the phase space area (A) divided by π, and has two conventionally used units: [mm $\cdot$ rad] and [$\pi \cdot$ mm $\cdot$ mrad],

$$\varepsilon = \frac{A}{\pi}. \tag{4.5}$$

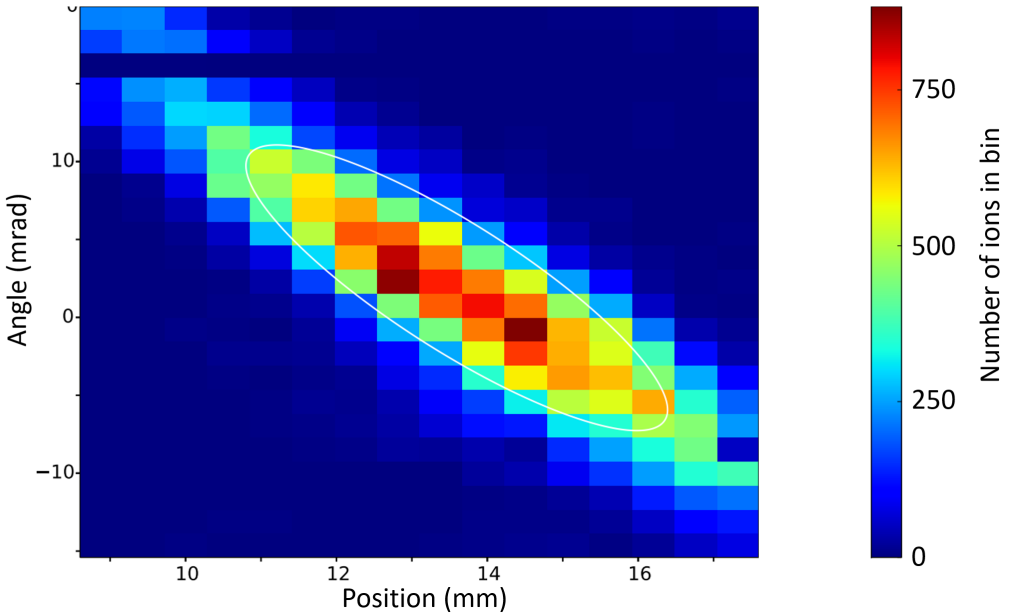

Figure 4.2: Measured EBIT extracted beam emittance. The rms emittance is outlined in white. $\varepsilon_{rms} = 8.47\ \pi \cdot \text{mm} \cdot \text{mrad}$, $x_{max} = 2.81$ mm, $\theta = 45°$, $E_{beam} = 2180$ eV/q. Figure from Ref. [60].

A beam in phase space typically has a Gaussian distribution and any definition of the emittance must define the amount of beam enclosed since a Gaussian distribution extends to infinity. This dissertation refers to rms emittance (ε_{rms}), defined as the area that encloses an emittance distribution at 1σ, divided by π (Figure 4.3). Units of [$\pi \cdot$ mm $\cdot$ mrad] are used due to the convenience of quoting a phase space area.

The collective shape of beam particles in phase space describes the behaviour of the beam. Emittance commonly has an elliptical shape that demonstrates the beam converging or diverging. Convergence and divergence are more easily interpreted in trace space where the axes are transverse position and the velocity vector's angle relative to the beam's longitudinal direction (x, x'), rather than position and momentum. Both phase and trace space have the same properties [63]. If the beam's semi-axes are parallel to the horizontal and vertical trace space axes, their lengths are equal to the beam radius and half the beam's angular divergence respectively.

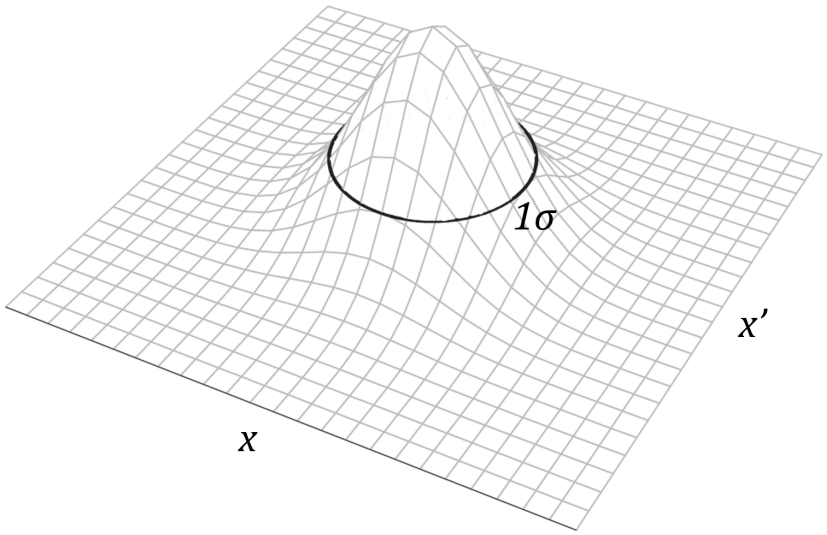

Figure 4.3: ε_{rms} Gaussian distribution. Figure adapted from Ref. [5].

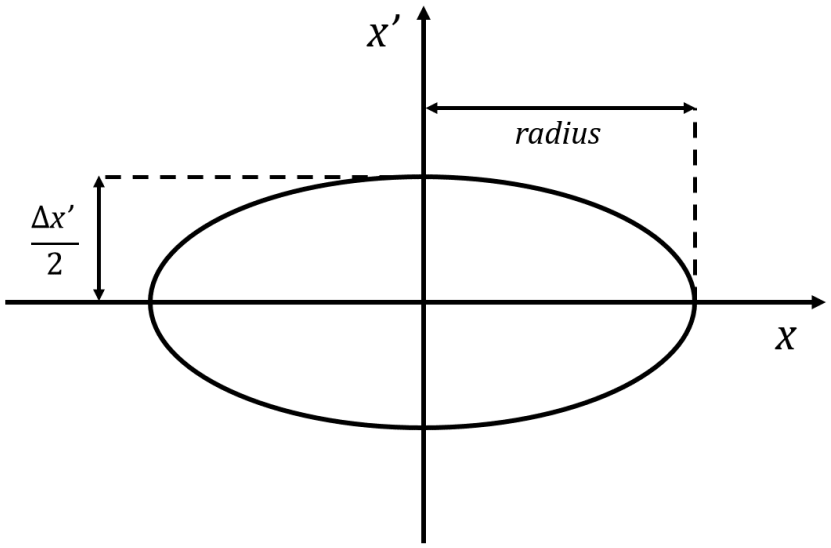

Figure 4.4: Emittance ellipse in trace space.

A clockwise tilted ellipse (with the trace space axis orientation in Figure 4.4) represents a converging beam since most velocity vectors are directed towards the longitudinal beam axis, resulting in a net convergence. Conversely, a counter-clockwise tilted beam represents a diverging beam as most velocity vectors are directed away from the longitudinal beam axis. A lens, therefore, rotates an emittance ellipse.

Under linear forces a particle in phase space will travel on its elliptical trajectory, thus by defining one large ellipse all particles within it will remain inside and the beam dynamics can be calculated by transforming the ellipse parameters of a single particle.

4.3.1 Twiss Parametrisation

An emittance ellipse can be defined by three parameters: phase space area (ε_{rms}), the length of a semi-axis and tilt angle (θ). The beam radius (x_{max}) is equal to the maximum position value of the particles, however the length of the semi-axis of a tilted emittance ellipse is not equal to the beam radius. Emittance ellipses are therefore also defined by the Twiss parametrisation [64]:

$$\varepsilon_{rms} \;=\; \gamma x^2 \;+\; 2\alpha x x' \;+\; \beta x'^2. \tag{4.6}$$

The Twiss parameters ($\gamma,\ \beta$ and α) are not physical quantities but are rather associated with the spatial extent, angular extent and inclination of the beam, respectively. The lengths of the semi axes are calculated independently.

$$x_{max} \;=\; \sqrt{\varepsilon\beta}\,, \tag{4.7}$$

$$x'_{max} \;=\; \sqrt{\varepsilon\gamma}\,, \tag{4.8}$$

$$\beta\gamma \;-\; \alpha^2 \;=\; 1\,, \tag{4.9}$$

$$\tan 2\theta \;=\; \frac{2\alpha}{\gamma \;-\; \beta}\,, \tag{4.10}$$

where x'_{max} is half the beam divergence.

β is easily obtained by measuring the beam radius and emittance, but γ requires

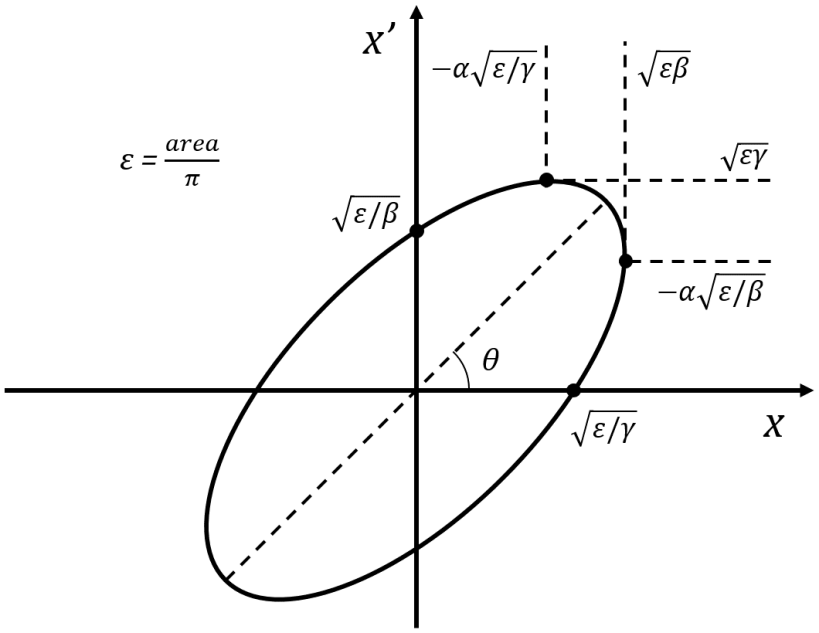

Figure 4.5: Twiss parametrisation ellipse definition.

further calculation. Solving Eqs. 4.9 and 4.10 for γ results in:

$$\begin{aligned}\gamma \;=\; \beta \;+\; 2\,\beta\cot^2(2\theta) \\ \pm\,\sqrt{2}\cot^2(2\theta)\,\sqrt{-\sec^2(2\theta)\;+\;2\,\beta^2\sec^2(2\theta)\;+\;\cos(4\theta)\sec^2(2\theta)}.\end{aligned} \tag{4.11}$$

The length of the semi-major axis must converge on x_{max} or x'_{max} at $\theta = 0$ and on infinity at $\theta = \pm\frac{\pi}{2}$, thus Eq. 4.11 only has one physical solution for any value of θ. The limits of γ are obtained from Figure 4.6 and are listed in Table 4.1. Eq. 4.11 is undefined at $\theta = 0, \pm\frac{\pi}{4}$, but for those orientations γ can be solved geometrically and is equal to $\frac{1}{\beta}$ and β when $\theta = 0$ and $\pm\frac{\pi}{4}$, respectively.

$\boldsymbol{\theta}$	0	$\pm\frac{\pi}{4}$	$\pm\frac{\pi}{2}$	$-\frac{\pi}{2} < \theta < -\frac{\pi}{4}$	$-\frac{\pi}{4} < \theta < \frac{\pi}{4}$, $\theta \neq 0$	$\frac{\pi}{4} < \theta < \frac{\pi}{2}$
$\boldsymbol{\gamma}$	$\frac{1}{\beta}$	β	∞	γ_+	γ_-	γ_+

Table 4.1: Twiss parameter γ boundary conditions. $\gamma_\pm$ is defined in Eq. 4.11.

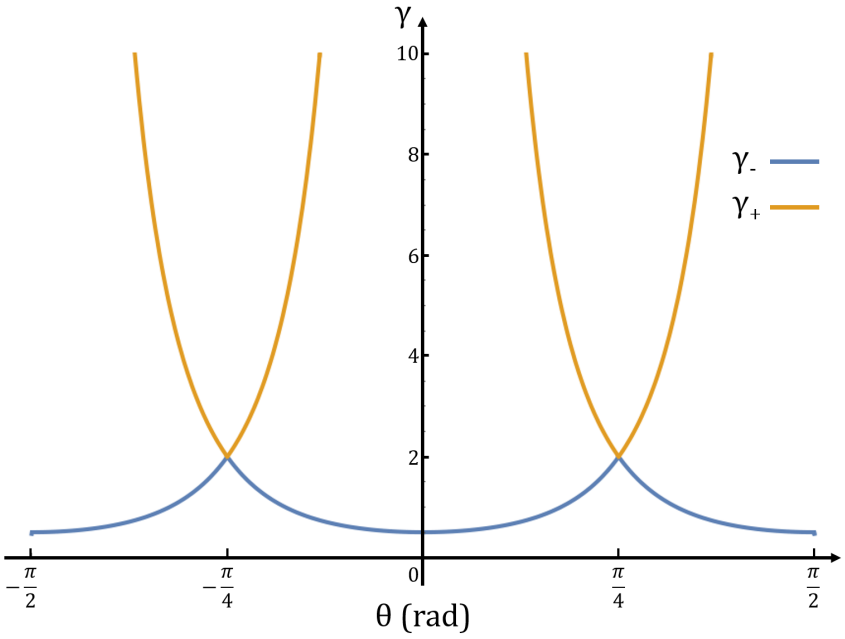

Figure 4.6: Twiss parameter γ solutions of Eq. 4.11 for $\beta = 2$.

The length of the semi-major (L) and minor (l) axes are dependent on β and γ [64]:

$$L = \sqrt{\frac{\varepsilon}{2}}(\sqrt{H+1} + \sqrt{H-1}), \tag{4.12}$$

$$l = \sqrt{\frac{\varepsilon}{2}}(\sqrt{H+1} - \sqrt{H-1}), \tag{4.13}$$

$$H = \frac{1}{2}(\gamma + \beta). \tag{4.14}$$

4.3.2 Emittance Calculations

For simulations to demonstrate processes that might realistically occur along the beam-line an appropriate beam must be defined. A program was therefore written to calculate the properties of individual ions in a beam with the measured emittance in Figure 4.2.

The beam spot and emittance distributions are each calculated from the two-dimensional

elliptical Gaussian probability density function:

$$f(x,y) = A\exp(-a(x-x_0)^2 + 2b(x-x_0)(y-y_0) - c(y-y_0)^2), \tag{4.15}$$

$$a = \frac{\cos^2(\theta)}{2\,{\sigma_x}^2} + \frac{\sin^2(\theta)}{2\,{\sigma_y}^2}, \tag{4.16}$$

$$b = \frac{\sin(2\theta)}{4\,{\sigma_y}^2} - \frac{\sin(2\theta)}{4\,{\sigma_x}^2}, \tag{4.17}$$

$$c = \frac{\sin^2(\theta)}{2\,{\sigma_x}^2} + \frac{\cos^2(\theta)}{2\,{\sigma_y}^2}, \tag{4.18}$$

where A is the amplitude, x_0, y_0 the centre in x and y axes respectively, θ the tilt angle, and σ_x, σ_y the x and y standard deviations. The standard deviations of an ε_{rms} ellipse are the semi-major and minor axes, calculated by Eq.s 4.12 and 4.13.

The volume under a two-dimensional probability density function is equal to the probability, thus the volume of Eq. 4.15 between infinite limits is equal to 1,

$$V = \int_{-\infty}^{\infty}\int_{-\infty}^{\infty} f(x,y)\,dxdy = 2\pi\,A\,\sigma_x\sigma_y = 1. \tag{4.19}$$

There is no analytical solution for finite intervals however, so the program calculates probabilities over finite intervals using numerical quadrature. Individual ion positions and velocity vectors are calculated from the probability distributions. A flowchart of the emittance calculation program is provided in Appendix A.

4.4 System Optimisation

A benefit of switchyard simulations is that issues along the beamline can be identified by introducing additional diagnostics. The switchyard diagnostics deficiency was rectified in the simulations by writing a user program to measure beam properties at defined planes. Measurement planes were positioned at apertures following components that change the

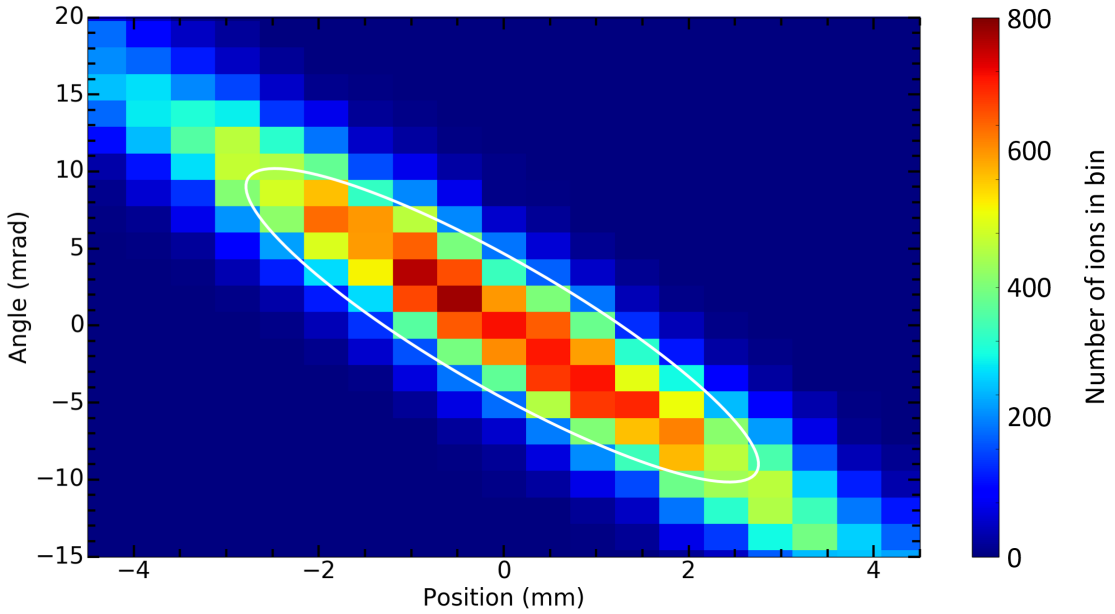

Figure 4.7: Calculated EBIT extracted beam emittance. The rms emittance is outlined in white. $\varepsilon_{rms} = 8.47\ \pi \cdot \text{mm} \cdot \text{mrad}$, $x_{max} = 2.81$ mm, $\theta = 45°$, $E_{beam} = 2180$ eV/q.

beam properties, and the central beam position, azimuthal and elevation incidence angles, emittance and transmission were all recorded. The system is optimised by sweeping through electrode potentials and plotting the corresponding beam properties. Optimum system parameters are identified by either a maximum transmission or a convergence of beam properties when they are coupled to multiple components. For example:

The potential of the EBIT injection/extraction steerer electrode could be optimised for extraction from the transmission at the upstream bender (B8 in Figure 4.9) which plateaus at 330 V (Figure 4.8a), but the beam properties at the quadrupoles are dependent on a combination of both steerer and bender potential values. The beam must be perpendicular to the quadrupole (Q5 in Figure 4.9) and enter on centre, the optimum electrode potentials are therefore when the position of the centre of the beam relative to the centre of the quadrupole, and the incidence angle are both zero for the same electrode potential configuration (Figure 4.8b).

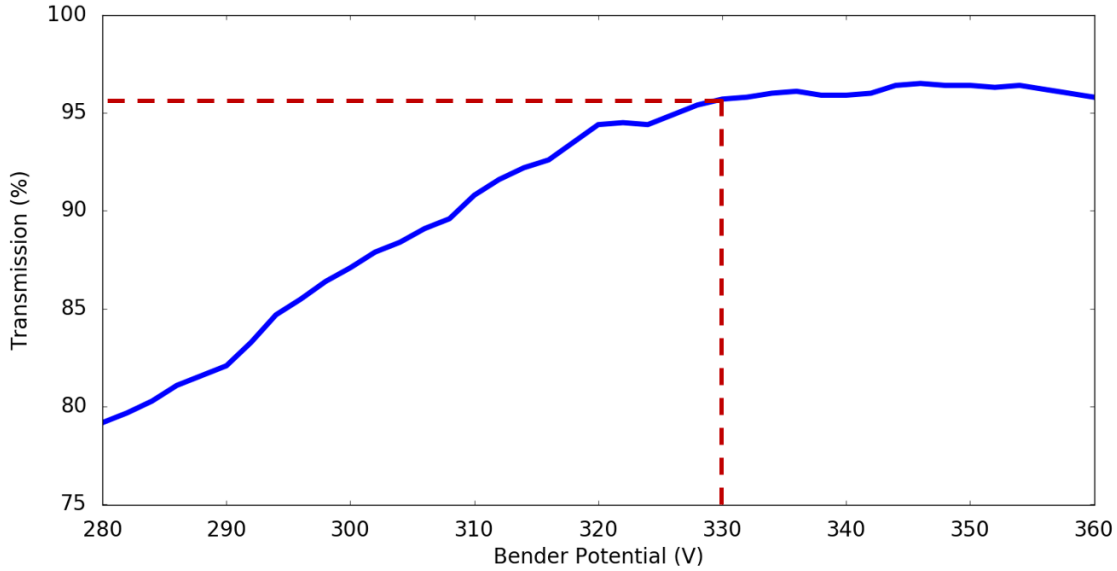

(a) Maximum transmission optimisation. The plateau in transmission at the bender upstream of the EBIT steerer from 330 V is indicated by the red line.

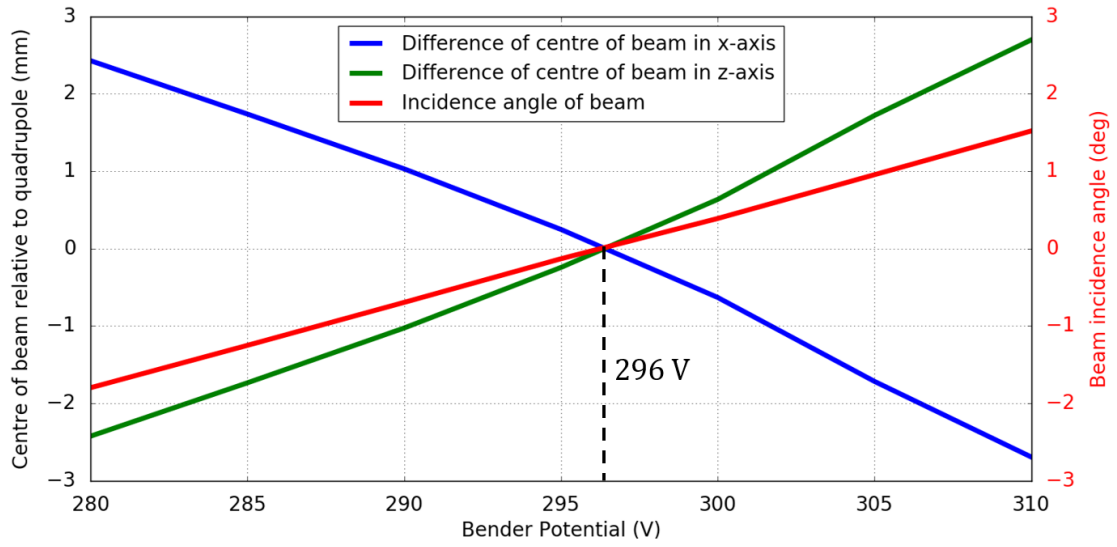

(b) Beam property convergence optimisation. The beam is both on-centre and perpendicular to the quadrupole aperture at the same electrode potential configurations. The steerer is at 323 V and the bender is at 296 V.

Figure 4.8: System optimisation methods.

Each element along the beamline is optimised in turn using this method, resulting in a maximum transmission at the MPET injection steerer. Despite an overall transmission

of 94.8 %, the idealistic simulation environment is not representative of a real beamline environment, so the observed transmission will still only be a fraction of the calculated transmission. The simulation of the system optimised for extraction of a $^{133}Cs^{17+}$ beam with the emittance in Figure 4.7 is shown in Figure 4.9 and its parameters listed in Table 4.2.

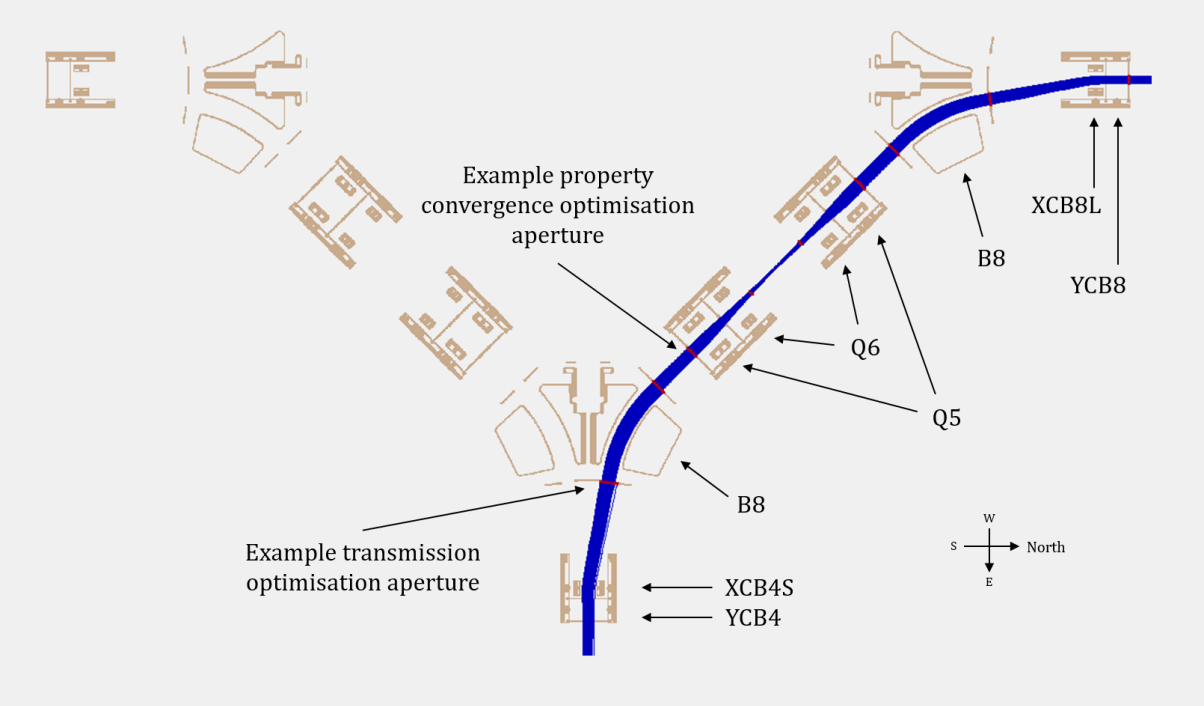

Figure 4.9: SIMION simulation of the TITAN switchyard optimised for extraction of $^{133}Cs^{17+}$ from the EBIT to MPET. Ion trajectories are displayed in blue, and measurement planes in red.

Electrode	YCB4	XCB4S	B8	Q5	Q6	XCB8L	YCB8
Potential (V)	160	323	296	216	227	323	160

Table 4.2: Optimised switchyard potentials for extraction of $^{133}Cs^{17+}$ from the EBIT.

Chapter 5

TITAN-EBIT High Voltage Upgrade

The design specifications of the TITAN-EBIT support a maximum operating voltage of 62 kV, but safety restrictions previously limited its operation to 7 kV. An upgrade of the EBIT high voltage operation was required for it to be safely operated at high voltages so as to create higher charge states of heavier ions necessary for investigations into decay rate modifications, and to increase the precision of TITAN mass measurements. Operating at 62 kV theoretically provides access to bare ions up to Z$\sim$65.

5.1 Design Brief

Consultations with high voltage experts, mechanical technicians and EBIT experimenters determined the content of the upgrade design brief:

- The system be approved for operation up to 65 kV.
- Internal sharp edges be rounded to a minimum radius of 30 mm, and a minimum separation allowance of 300 V/mm between grounded and biased surfaces be maintained to reduce the electric fields.
- Access to high voltage components be restricted to prevent personnel entry before the risks have been minimised.
- Overhead access to the trap and detectors not to be obstructed.

5.2 Previous System Appraisal

An evaluation of the previous EBIT configuration determined that operation at its maximum design specification would be inherently unsafe. The configuration comprised floated pipes containing high voltage cables, enclosed in grounded ducts that formed a single Faraday cage running from a power supply rack to both the electron gun and collector, but contained features that did not adhere to TRIUMF safety regulations.

The most immediate safety issues were the ground to bias separation distances since floated pipes and electron gun manipulator manual controls were too close to grounded duct surfaces. Separating the pipes and ducts were epoxy insulators which, despite being predominantly made of an insulating material, featured metal sections that reduced the minimum separation distance. The pipes also featured a hazardous airgap between their biased PVC surface and aluminium coating.

TRIUMF electrical safety regulations require that no unauthorised or unsafe access to enclosures at high voltage is possible. As a precaution, lockout procedures should be implemented to restrict access, but in the previous system setup no locks prevented access to either the cage or the collector whilst at high voltage. Holes in enclosures were also big enough to potentially allow objects to be inserted into the cage and short the rack to ground.

5.3 Upgrade Design

Having identified the problems present in the previous system setup, the upgrade design proposed solutions to make the EBIT safe for high voltage operation. An overview of the design is displayed in Figure 5.1.

Connecting the electron gun and collector to the pre-approved power supply rack en-

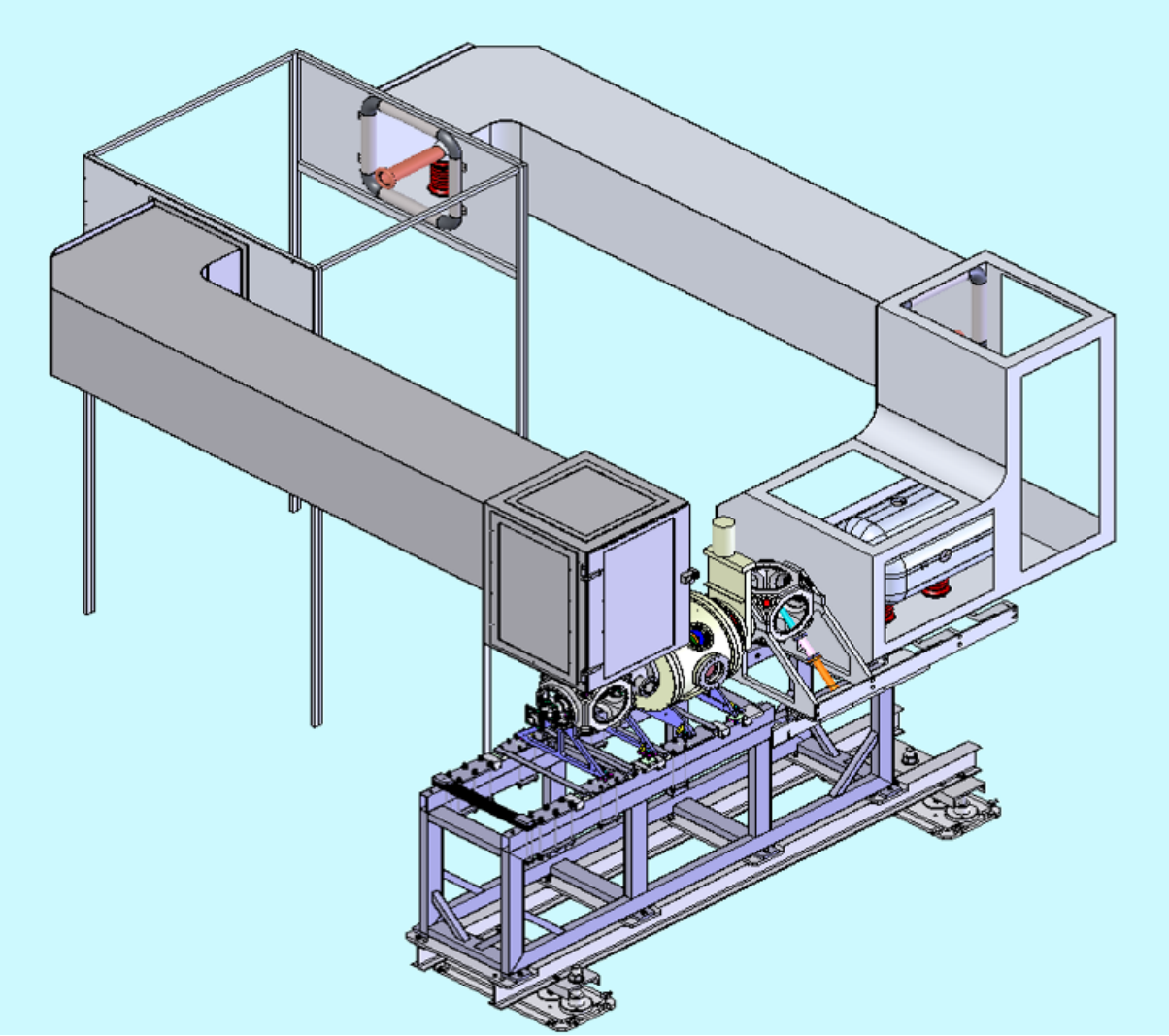

Figure 5.1: Upgrade design model. An outline of the pre-approved power supply rack enclosure is shown. Model from Refs. [55, 65, 66].

closure creates a single Faraday cage, as shown by the schematic in Figure 5.2.

5.3.1 Reduced Electric Fields

Based on an advised separation allowance of 300 V/mm, the minimum separation distance between ground and any surface biased to 65 kV is 0.217 m. For additional safety, other than for fixed height insulators (0.222 m) a minimum separation distance of 0.229 m is maintained.

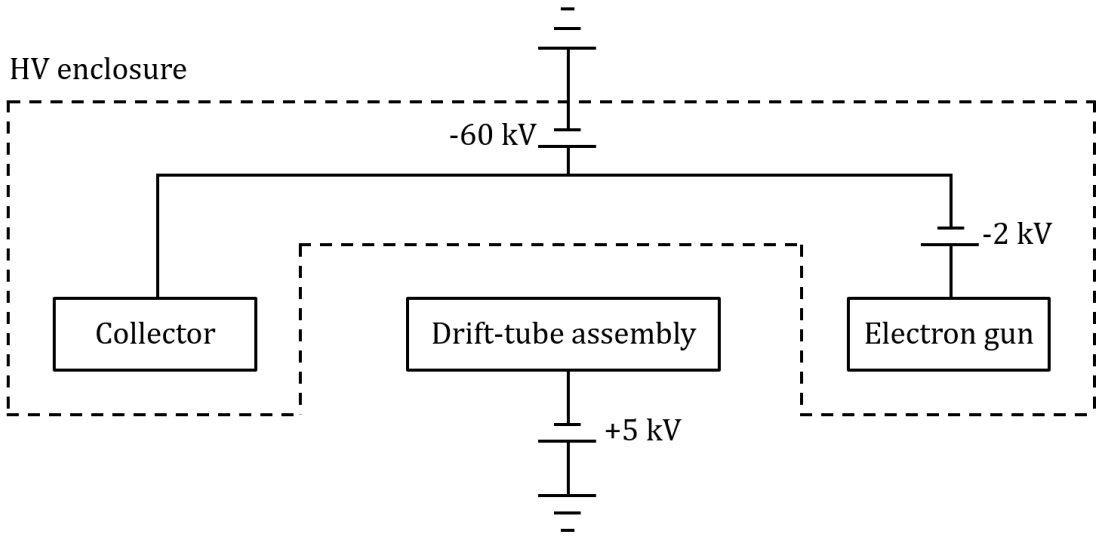

Figure 5.2: High voltage enclosure Faraday cage schematic.

Due to the resultant singularity in electron charge distribution at sharp edges, all edges within a high voltage enclosure must be rounded to a minimum radius of 30 mm. The upgrade therefore features corona guards at pipe and duct ends, and rounded end-caps that secure the pipes to the insulators. The complexity of the fields at the electron gun manipulator required that the whole manipulator have its own enclosure (Figure 5.3).

5.3.2 Restricted Access

A lockout procedure requiring the power supply be turned off and grounded, and any surface previously at high voltage be grounded before an enclosure can be opened is implemented to ensure that no unauthorised or unsafe access to high voltage enclosures is possible. The chain also includes a key to be kept by personnel working in an enclosure to ensure that the power supply cannot be turned on whilst work is being performed on the system. A diagram of the interlock chain is provided in Appendix B.

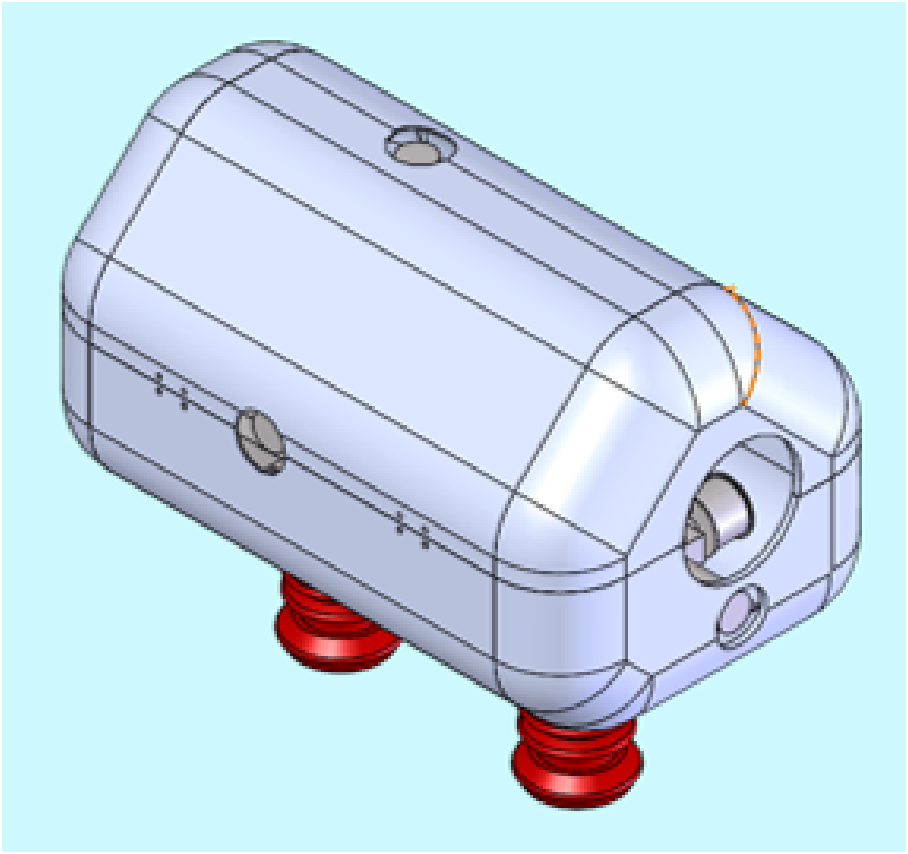

Figure 5.3: Electron gun manipulator individual enclosure. Figure from Ref. [65].

5.4 Design Review

The design was reviewed by a panel of high voltage experts, mechanical technicians and EBIT experimenters, who approved proceeding to manufacturing providing a number of features were adapted prior to commissioning. The conditions of approval were that due diligence must be demonstrated by ensuring that unauthorised access to enclosures is challenging, and that safety warnings highlighting potential dangers must be clearly visible. A structural engineer must also evaluate the upgrade and determine that it is suitable to safely withstand an earthquake.

5.5 Assembly and Installation

Manufacturing began on-site at TRIUMF in early August 2016, whilst the previous setup was disassembled in parallel.

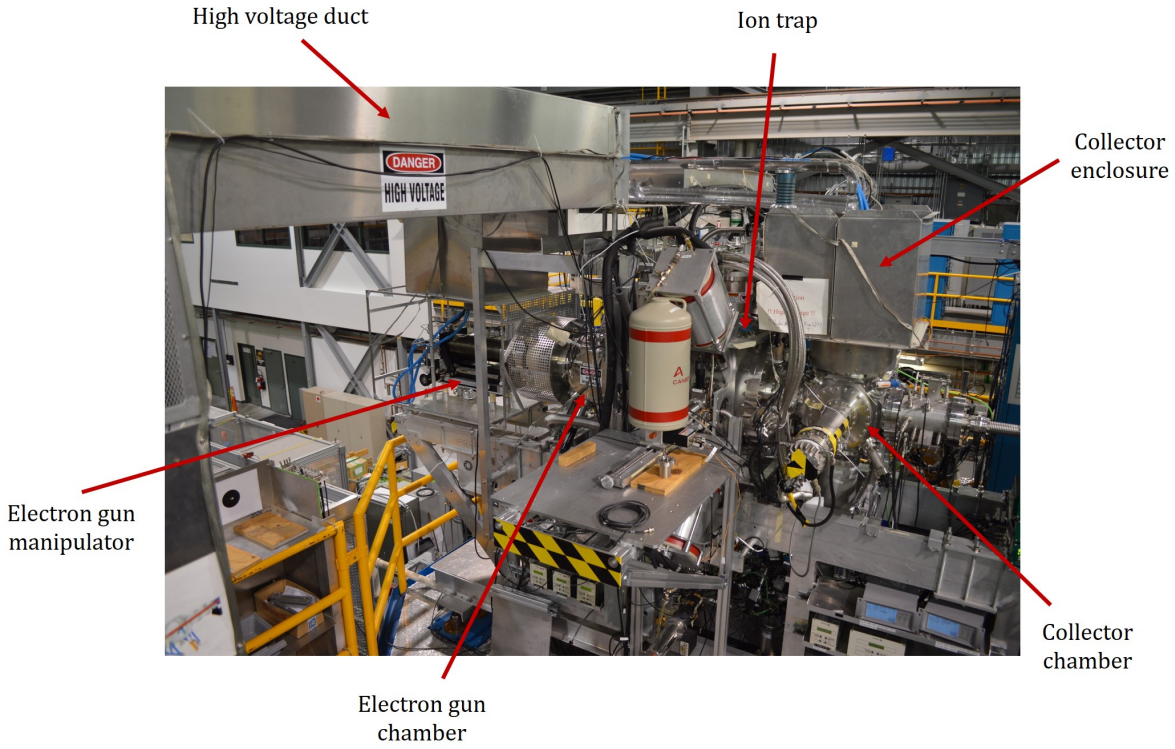

Figure 5.4: Disassembly of the previous setup.

Where possible, new parts were assembled off the TITAN platform so as to be craned into position as a complete single component later in the process. The electron gun and collector ducts were the first parts to be fully assembled, with the pipes secured to the insulators with rounded endcaps, and corona guards rounding off the sharp pipe ends.

5.5.1 System Adjustments

The increased separation distances introduced by the new gun-supporting insulators required the installation of new support rails on which the electron gun, chamber and its enclosure would be mounted (Figure 5.6). Upon mounting the gun enclosure on the new rails, a rotation of the EBIT around its beamline that resulted in a misalignment of the EBIT and support structure horizontal axes was discovered. The misalignment was cor-

(a) Duct interior with pipe, insulators and endcaps.

(b) Corona guard on sharp pipe end.

Figure 5.5: First fully assembled parts, assembled off the TITAN platform and later craned into position as a single complete component.

rected by raising or lowering the respective sides of the whole EBIT by equal amounts, maintaining all alignments within the trap.

Upstream of the trap are four ports for trap feedthroughs, equally spaced around the

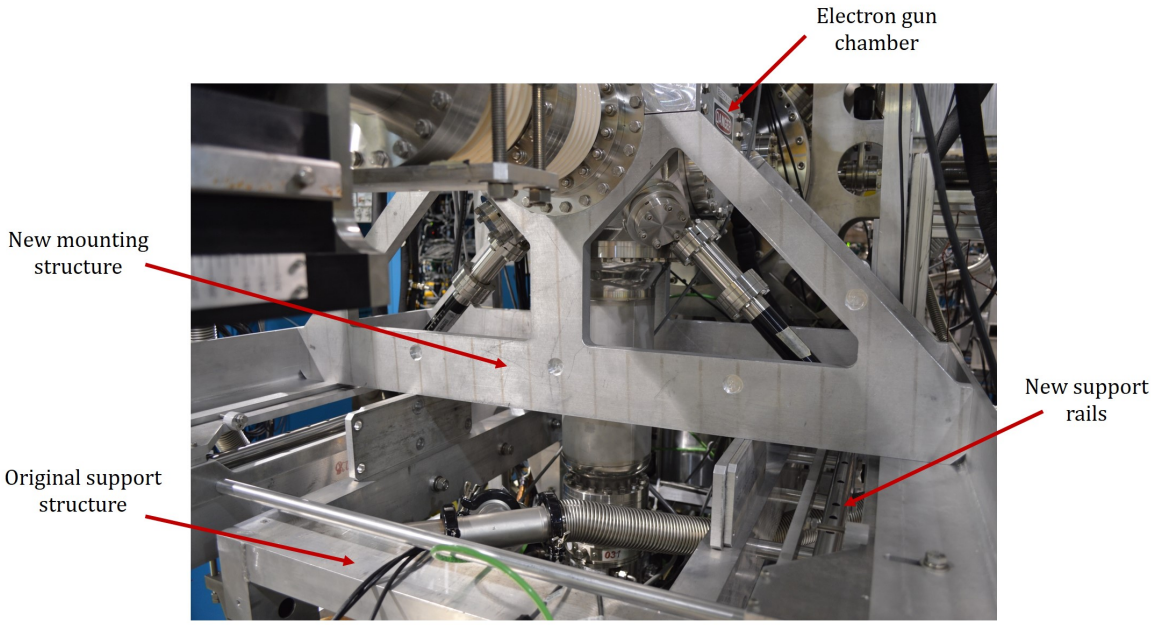

Figure 5.6: Installation of new support rails on which the electron gun, chamber and enclosure are mounted.

longitudinal axis. A rotation of all ports by 45° around the beamline was necessary to avoid physical interference with the new collector enclosure.

5.5.2 Completion

Following the installation of the gun and collector enclosures, the assembled ducts were craned into position to connect them to the power supply rack. Cables were fed through the pipes and reconnected, the final corona guards added, and small final features such as door hinges installed. Full installation of the upgrade of the TITAN-EBIT high voltage operation was completed in mid-December 2016.

(a) Gun and collector ducts and gun enclosure.

(b) Collector enclosure.

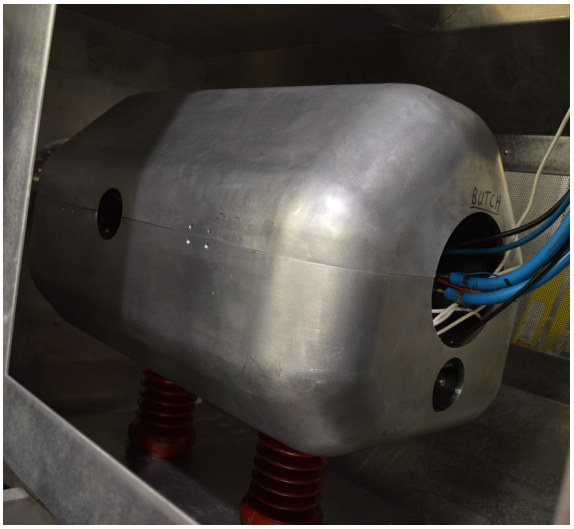

(c) Gun manipulator enclosure.

Figure 5.7: Overview of the completed upgrade.

Chapter 6

Conclusions & Future Work

The objective of the project to upgrade the TITAN-EBIT high voltage operation was to install a new system that permitted operation at the maximum design specification. Operation at higher voltages creates the higher charge states necessary for investigations into decay rate modifications, and a reduction in MPET mass measurement uncertainties. The upgrade was fully installed in mid-December 2016, and the accompanying switch-yard simulations also completed. Further work prior to full commissioning in early 2017 includes minor adjustments and the final HV expert review process. The power supply rack will be altered to eliminate all sharp edges and ensure that minimum separation distances are maintained, and the capacitance of the transformer will be measured to determine if the transformer and power supply each need new enclosures. The final review is expected to be in the first quarter of 2017 during which approval of operation must be granted before the group can proceed with commissioning. Until then TITAN is still able to continue with experiments involving lower energy charge breeding that were possible with the previous configuration.

Following commissioning the system could be immediately operated at its maximum specification. As a result the outstanding requirements of experiments S1478 [11] and S1695 [51] will have been fulfilled and TITAN could theoretically proceed to measure the Ne-, He- and H-like charge states of ^{64}Cu, and utilise $0^+ \rightarrow 0^+$ transitions to probe

2-photon decays of bare $^{98}Zr^{40+}$ and $^{98}Mo^{42+}$. Future upgrades include a new power supply and the installation of a 5 A electron gun that will create high charge states of even heavier ions.

Although the upgrade does not yet have approval to go to 62 kV the process has already proven to be instrumental in the improvement of the TITAN-EBIT. The work has identified and solved problems such as the axis misalignment between the EBIT and its support structure, and highlighted inherently dangerous features of the previous setup. Preliminary assessments indicate that high voltage approval will be granted in the near future, and the TITAN-EBIT will start to explore a new compelling area of nuclear physics.

APPENDICES

Appendix A

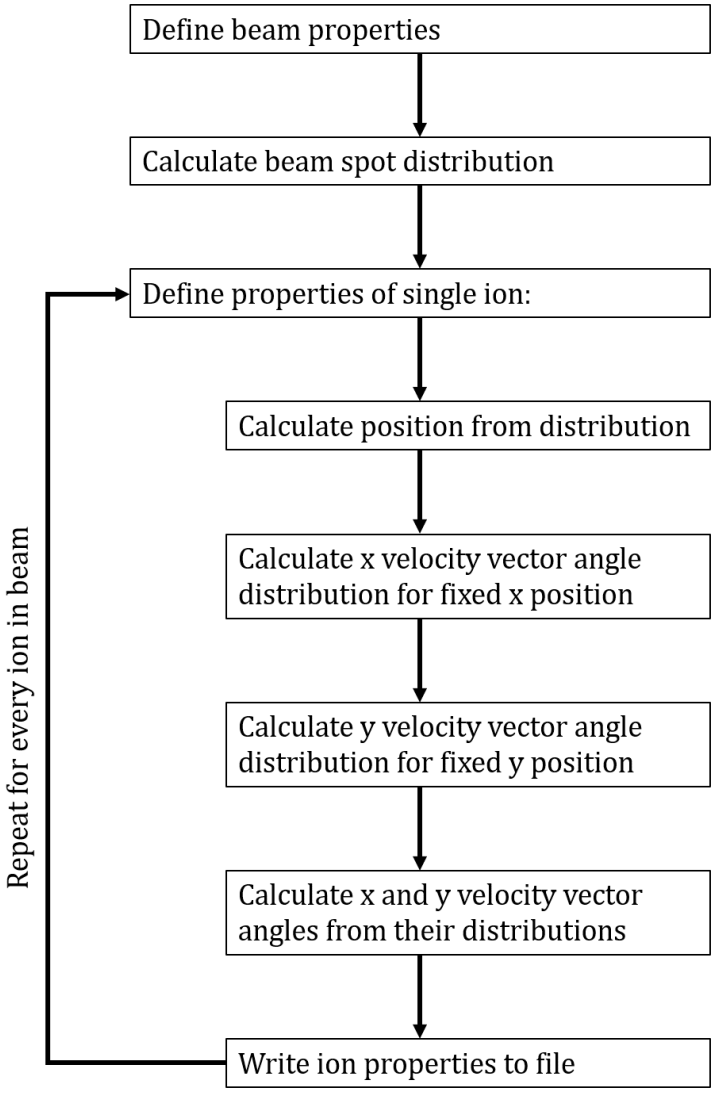

Figure A.1: Calculated emittance program flowchart.

Appendix B

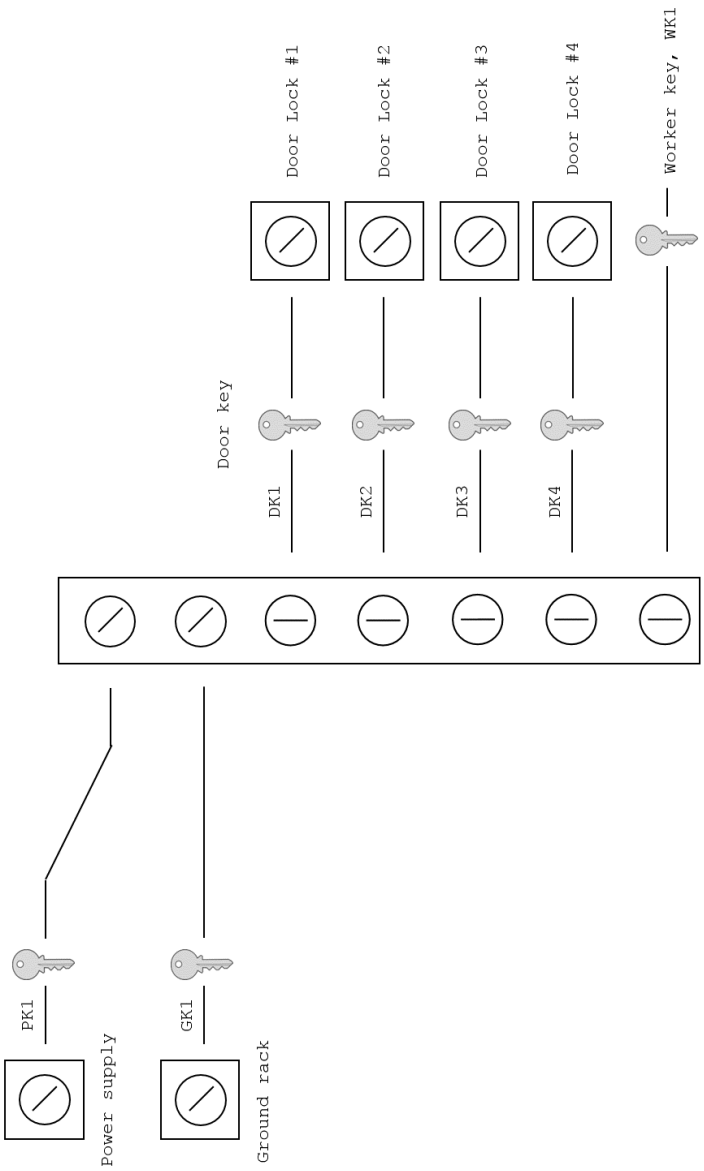

Figure B.1: Lockout procedure. Locks at 45° require turning, whilst locks parallel to their box will only release their keys when all keys are present.

Bibliography

[1] TRIUMF. http://www.triumf.ca. Online; accessed 09-2016.

[2] A. Lennarz, *In-trap decay spectroscopy on highly-charged radioactive ions towards measurements on intermediate nuclei in $\beta\beta$ decay.* PhD thesis, Westfälische Wilhelms-Universität Münster, 2015.

[3] M. Marchetto *et al.*, "ARIEL front end," in *ISAC and ARIEL: The TRIUMF Radioactive Beam Facilities and the Scientific Program* (J. Dilling, R. Krücken, and L. Merminga, eds.), pp. 275–282, Springer, 2014.

[4] D. Lascar, A. Kwiatkowski, *et al.*, "Improvements to TITAN's mass measurement and decay spectroscopy capabilities," *Nuclear Instruments and Methods in Physics Research B*, vol. 376, pp. 292–297, 2016.

[5] M. Smith, "A Square Wave Driven Linear Paul Trap for TITAN," Master's thesis, University of British Columbia, 2004.

[6] J. Dilling *et al.*, "ISAC Overview," in *ISAC and ARIEL: The TRIUMF Radioactive Beam Facilities and the Scientific Program* (J. Dilling, R. Krücken, and L. Merminga, eds.), pp. 1–8, Springer, 2014.

[7] P. Bricault *et al.*, "Rare isotope beams at ISAC-target & ion source systems," in *ISAC and ARIEL: The TRIUMF Radioactive Beam Facilities and the Scientific Program* (J. Dilling, R. Krücken, and L. Merminga, eds.), pp. 25–49, Springer, 2014.

[8] M. Brodeur, V. L. Ryjkov, *et al.*, "Verifying the accuracy of the TITAN Penning-trap mass spectrometer," *International Journal of Mass Spectrometry*, vol. 310, pp. 20–31, 2012.

[9] TITAN. http://titan.triumf.ca. Online; accessed 09-2016.

[10] P. Delheij, L. Blomeley, M. Froese, *et al.*, "The TITAN mass measurement facility at TRIUMF ISAC," *Hyperfine Interactions*, vol. 173, pp. 123–131, 2006.

[11] K. Leach, I. Dillmann, R. Klawitter, and J. Dilling, "Investigating Electron Capture Rates of Highly-Charged Ions." TRIUMF EEC proposal S1478, 2014.

[12] M. Brodeur *et al.*, "New mass measurement of 6Li and ppb-level systematic studies of the Penning trap mass spectrometer TITAN," *Physical Review C*, vol. 80, 2009.

[13] M. Mukherjee *et al.*, "ISOLTRAP: An on-line Penning trap for mass spectrometry on short-lived nuclides," *The European Physical Journal A*, vol. 35, pp. 1–29, 2008.

[14] A. Lapierre *et al.*, "The TITAN EBIT charge breeder for mass measurements on highly charged short-lived isotopes - First online operation," *Nuclear Instruments and Methods in Physics Research A*, vol. 624, p. 54, 2010.

[15] G. Savard, S. Becker, G. Bollen, H. J. Kluge, R. B. Moore, L. Schweikhard, H. Stolzenberg, and U. Wiess, "A new cooling technique for heavy ions in a Penning trap," *Physics Letters A*, vol. 158, pp. 247–252, 1991.

[16] V. V. Simon *et al.*, "A cooler Penning trap for the TITAN on-line trapping facility," *Journal of Physics: Conference Series*, vol. 312, 2011.

[17] G. Choppin, *Radiochemistry and Nuclear Chemistry*. Academic Press, 2013.

[18] K. Krane, *Introductory Nuclear Physics*. Wiley, 1988.

[19] Y. Litvinov and F. Bosch, "Beta decay of highly charged ions," *Reports on Progress in Physics*, vol. 74, p. 016301, 2011.

[20] E. Fermi, *Nuclear Physics*. University of Chicago Press, 1950.

[21] L. Folan and V. Tsifrinovich, "Effects of the Hyperfine Interaction on Orbital Electron Capture," *Physical Review Letters*, vol. 74, pp. 499–501, 1995.

[22] S. Wong, *Introductory Nuclear Physics*. Wiley-VCH, 2004.

[23] S. Barwick, J. Beacom, *et al.*, "APS Neutrino Study: Report of the Neutrino Astrophysics and Cosmology Working Group." http://www.aps.org/policy/reports. Online; accessed 10-2016.

[24] Y. Mochizuki *et al.*, "^{44}Ti: its effective decay rate in young supernova remnants, and its abundance in Cassiopeia A," *Astron. Astrophys.*, vol. 346, pp. 831–342, 1999.

[25] G. T. Emery, "Perturbation of nuclear decay rates," *Annual Review Nuclear Science*, vol. 22, pp. 165–202, 1972.

[26] D.Müller, "Direct observations of galactic cosmic rays," *The European Physical Journal H*, vol. 37, pp. 413–458, 2012.

[27] J. S. George, K. A. Lave, M. E. Wiedenbeck, *et al.*, "Elemental Composition and Energy Spectra of Galactic Cosmic Rays during Solar Cycle 23," *The Astrophysical Journal*, vol. 698, pp. 1666–1681, 2009.

[28] E. Stone, C. Cohen, W. Cook, *et al.*, "The Cosmic-Ray Isotope Spectrometer for the Advanced Composition Explorer," *Space Science Reviews*, vol. 86, pp. 285–356, 1998.

[29] G. Audi, F. G. Kondev, M. Wang, B. Pfeiffer, X. Sun, J. Blachot, and M. MacCormick, "The Nubase2012 evaluation of nuclear properties," *Chinese Physics C*, vol. 36, 2012.

[30] R. von Steiger, G. Gloeckler, and G. Mason, "The Composition of Matter," *Space Sciences Series of ISSI*, vol. 27, 2007.

[31] D. Atanasov *et al.*, "Between atomic and nuclear physics: radioactive decays of highly-charged ions," *Journal of Physics B: Atomic, Molecular and Optical Physics*, vol. 48, no. 14, 2015.

[32] Y. A. Litvinov *et al.*, "Measurement of the β^+ and Orbital Electron-Capture Decay Rates in Fully Ionized, Hydrogen-like, and Helium-like ^{140}Pr Ions," *Physical Review Letters*, vol. 99, p. 262501, 2007.

[33] N. Winckler, H. Geissel, Y. A. Litvinov, *et al.*, "Orbital electron capture decay of hydrogen- and helium-like ^{142}Pm ions," *Physics Letters B*, vol. 679, pp. 36–40, 2009.

[34] D. R. Atanasov, N. Winckler, *et al.*, "Half-life measurements of stored fully ionized and hydrogen-like ^{122}I ions," *The European Physical Journal A*, vol. 48, pp. 22–28, 2012.

[35] Z. Patyk, J. Kurcewicz, F. Bosch, H. Geissel, Y. A. Litvinov, and M. Pfützner, "Orbital electron capture decay of hydrogen- and helium-like ions," *Physical Review C*, vol. 77, 2008.

[36] C. N. Davids, A. J. Elwyn, B. W. Filiponne, *et al.*, "Branching ratio in the electron-capture decay of ^{7}Be," *Physical Review C*, vol. 28, no. 2, 1983.

[37] J. L. Osborne, C. A. Barnes, R. W. Kavanagh, R. M. Kremer, G. J. Mathews, J. L. Zyskind, P. D. Parker, and A. J. Howard, "Low-Energy ^{3}He$(\alpha,\gamma)^7$Be Cross-Section Measurements," *Physical Review Letters*, vol. 48, 1982.

[38] M. F. Altmann, R. L. Mößbauer, and L. J. N. Oberauer, "Solar neutrinos," *Reports on Progress in Physics*, vol. 64, pp. 97–146, 2001.

[39] J. N. Bahcall, A. M. Serenelli, and S. Basu, "New Solar Opacities, Abundances, Helioseismology, and Neutrino Fluxes," *The Astrophysical Journal Letters*, vol. 621, no. 1, 2005.

[40] F. Nolden, F. Bosch, K. Beckert, B. Franzke, O. Klepper, C. Kozhuharov, G. Menzel, R. Moshammer, H. Reich, B. Schlitt, M. Steck, T. Winkler, T. Faestermann, J. Friese, F. Heine, P. Kienle, E. Wefers, K. Zeitelhack, and K. Takahashi, "Half-life measurement of the bound state beta decay of ^{187}re^{75+}," *Nuclear Physics A*, vol. 621, no. 1, pp. 297 – 304, 1997.

[41] M. Jung, F. Bosch, K. Beckert, H. Eickhoff, H. Folger, B. Franzke, A. Gruber, P. Kienle, O. Klepper, W. Koenig, C. Kozhuharov, R. Mann, R. Moshammer, F. Nolden, U. Schaaf, G. Soff, P. Spädtke, M. Steck, T. Stöhlker, and K. Sümmerer, "First observation of bound-state β^- decay," *Physical Review Letters*, vol. 69, pp. 2164–2167, 1992.

[42] K. Takahashi and K. Yokoi, "Nuclear β-Decays of Highly Ionized Heavy Atoms in Stellar Interiors," *Nuclear Physics A*, vol. 404, pp. 578–598, 1983.

[43] K. Yokoi, K. Takahashi, and M. Arnould, "The ^{187}Re-^{187}Os Chronology and Chemical Evolution of the Galaxy," *Astronomy & Astrophysics*, vol. 117, pp. 65–82, 1983.

[44] F. Bosch, T. Faestermann, J. Friese, F. Heine, P. Kienle, E. Wefers, K. Zeitelhack, K. Beckert, B. Franzke, O. Klepper, C. Kozhuharov, G. Menzel, R. Moshammer, F. Nolden, H. Reich, B. Schlitt, M. Steck, T. Stöhlker, T. Winkler, and K. Takahashi, "Observation of Bound-State β Decay of Fully Ionized ^{187}Re: ^{187}Re^{187}Os Cosmochronometry," *Physical Review Letters*, vol. 77, 1996.

[45] Z. Chen, L. Rosenberg, and L. Spruch, "Hartree-Fock calculations of the ratio of bound-state to continuum beta decay of ^{187}Re, the chronometric partner of ^{187}Os," *Physical Review A*, vol. 35, 1981.

[46] K. Takahashi, R. N. Boyd, G. J. Mathews, and K. Yokoi, "Bound-state beta decay of highly ionized atoms," *Physical Review C*, vol. 36, 1987.

[47] H. Irnich, H. Geissel, F. Nolden, *et al.*, "Half-Life Measurements of Bare, Mass-Resolved Isomers in a Storage-Cooler Ring," *Physical Review Letters*, vol. 75, no. 23, 1995.

[48] Y. Litvinov *et al.*, "Observation of a dramatic hindrance of the nuclear decay of isomeric states for fully ionized atoms," *Physics Letters B*, vol. 573, no. 9, pp. 80–85, 2003.

[49] A. Akber *et al.*, "Increased isomeric lifetime of hydrogen-like ^{192m}Os," *Physical Review C*, vol. 91, 2015.

[50] F. Attallah, M. Aiche, J. Chemin, J. Scheurer, W. E. Meyerhof, J. Grandin, *et al.*, "Charge State Blocking of K-Shell Internal Conversion in ^{125}Te," *Physical Review Letters*, vol. 75, no. 9, 1995.

[51] E. Leistenschneider, K. G. Leach, and J. Dilling, "Nuclear Two-Photon Emission Unveiled Through Suppression of First-Order Decay Processes." TRIUMF EEC proposal S1695, 2016.

[52] C. Nociforo, F. Farinon, A. Musumarra, *et al.*, "Measurements of α-decay half-lives at GSI," *Physica Scripta*, vol. T150, 2012.

[53] R. Marrs, P. Beiersdörfer, and D. Schneider, "The Electron-Beam Ion Trap," *Physics Today*, vol. 47, pp. 27–34, 1994.

[54] F. Currell, B. O'Rourke, and H. Watanabe, "Design of an electron-beam ion trap to be situated at Queen's University, Belfast," *Review of Scientific Instruments*, vol. 75, pp. 1551–1553, 2004.

[55] Max-Planck-Institut für Kernphysik, "uebersicht_total." Solidworks 2014 Model, 2016.

[56] F. Currell and G. Fussmann, "Physics of Electron Beam Ion Traps and Sources," *IEEE Transactions on Plasma Science*, vol. 33, pp. 1763–1777, 2005.

[57] M. Froese, "The TITAN Electron Beam Ion Trap: Assembly, Characterization, and First Tests," Master's thesis, University of Manitoba, 2006.

[58] A. Lennarz, A. Grossheim, K. Leach, *et al.*, "In-Trap Spectroscopy of Charge-Bred Radioactive Ions," *Physical Review Letters*, vol. 113, 2014.

[59] D. Manura and D. Dahl, *SIMION (R) 8.0/8.1 User Manual*. Scientific Instrument Services, Inc., 2011.

[60] R. Schupp, "Determination of beam properties of highly-charged ions extracted from TITANs electron beam ion trap," Master's thesis, Universität Heidelberg, 2016.

[61] A. Wolski, *Beam Dynamics in High Energy Particle Accelerators*. ICP, 2014.

[62] H. Wiedemann, *Particle Accelerator Physics*. Springer-Verlag Berlin Heidelberg, 2007.

[63] J. Buon, "Beam Phase Space and Emittance." CAS - CERN Accelerator School: 5th Gneral Accelerator Physics Course, CERN-1994-001, DOI 10.5170/CERN-1994-001.89.

[64] P. H. Dawson, *Quadrupole Mass Spectrometry and Its Applications*. AIP-Press, 1995.

[65] M. Good and TRIUMF, "Assembly: IEX1932." TRIUMF, 2016.

[66] M. Good and TRIUMF, "riggingassembly." Solidworks 2014 Model, 2016.